Published for the International Glaciological Society

THIS MANUSCRIPT HAS BEEN SUBMITTED TO THE JOURNAL OF GLACIOLOGY AND HAS NOT BEEN PEER-REVIEWED.

Multi-component Rayleigh wave dispersion analysis

Journal:	*Journal of Glaciology*
Manuscript ID	JOG-2025-0090
Manuscript Type:	Article
Date Submitted by the Author:	26-Jun-2025
Complete List of Authors:	Garvey, Samara; Colorado School of Mines Department of Geophysics Siegfried, Matthew; Colorado School of Mines, Department of Geophysics Shragge, Jeff; Colorado School of Mines Department of Geophysics Zoet, Lucas; University of Wisconsin-Madison, Geoscience Hansen, Dougal; Washington University in St Louis Stevens, Nathan; University of Washington, Pacific Northwest Seismic Network
Keywords:	Glacier geophysics, Glaciological instruments and methods, Seismology
Abstract:	Seismic ice velocity estimates provide quantitative constraints on glacial systems including ice thickness, englacial structure, and bedrock topography. Detailed velocity modeling using active-source seismic surveys on glaciers, however, is often challenged by sub-optimal survey acquisition design due to complex field logistics. This study explores new potential of such surveys for characterizing potentially heterogeneous seismic ice velocities by leveraging dispersive Rayleigh-wave responses recorded on three-component (3-C) receivers. We use synthetic models to study survey design, data conditioning, and improvements provided by multi-component data for dispersion analysis that inform estimates of vertical velocity profiles. We employ these learnings to optimize the accuracy of dispersion curves derived from a limited aperture, 3-C dataset acquired on the Saskatchewan Glacier in the Canadian Rocky Mountains. Our experiments suggest that when working with a limited number of geophones practitioners should: prioritize array length over finer receiver spacing; use shot points to infill receiver gaps; preprocess

	shot-gather data to emphasize Rayleigh waves; and use supergathers to enhance signal-to-noise ratio and extend effective array aperture prior to building dispersion panels. Finally, we extract novel value from 3-C dispersion analysis by combining vertical- and horizontal-displacement data to reduce uncertainty and improve picked dispersion curve accuracy.

Multi-component Rayleigh wave dispersion analysis

Samara M. GARVEY,[1] Matthew R. SIEGFRIED,[1] Jeffrey SHRAGGE,[1] Lucas ZOET,[2] Dougal HANSEN,[3] Nathan T. STEVENS[4]

[1]*Department of Geophysics, Colorado School of Mines, Golden, 80401, CO, USA*

[2]*Department of Geoscience, University of Wisconsin–Madison, Madison, 53706, WI, USA*

[3]*Department of Earth, Environmental, and Planetary Sciences, Washington University, St. Louis, MO, 63130*

[4]*Pacific Northwest Seismic Network, University of Washington, Seattle, WA, USA*

Correspondence: Samara Omar <somar@mines.edu>

ABSTRACT. Seismic ice velocity estimates provide quantitative constraints on glacial systems including ice thickness, englacial structure, and bedrock topography. Detailed velocity modeling using active-source seismic surveys on glaciers, however, is often challenged by sub-optimal survey acquisition design due to complex field logistics. This study explores new potential of such surveys for characterizing potentially heterogeneous seismic ice velocities by leveraging dispersive Rayleigh-wave responses recorded on three-component (3-C) receivers. We use synthetic models to study survey design, data conditioning, and improvements provided by multi-component data for dispersion analysis that inform estimates of vertical velocity profiles. We employ these learnings to optimize the accuracy of dispersion curves derived from a limited aperture, 3-C dataset acquired on the Saskatchewan Glacier in the Canadian Rocky Mountains. Our experiments suggest that when working with a limited number of geophones practitioners should: prioritize array length over finer receiver spacing; use shot points to infill receiver gaps; preprocess shot-gather data to emphasize Rayleigh waves; and use supergathers to enhance signal-to-noise ratio and extend effective array aperture prior to building dispersion panels. Finally, we extract novel value from 3-C dispersion analysis by combining vertical- and horizontal-displacement data to reduce uncertainty and

improve picked dispersion curve accuracy.

INTRODUCTION

The structure and material properties of ice masses and underlying bedrock are key parameters that control ice flow (e.g., Bennett, 2022). Active-source seismic methods, which operate at low (sub-200 Hz) frequencies (Podolskiy and Walter, 2016), allow for deep subsurface investigations (e.g., at the ice-bedrock interface and internal bedrock layering) by using a controlled source of acoustic waves, which are sensitive to variations in compressional- (P) and shear- (S) wave velocities and density of the elastic medium. This method has been leveraged to map subglacial structures across multiple glacier types (typically using reflected or refracted wave data), such as at Rutford Ice Stream in West Antarctica (Smith, 1997) and the Taku (Zechmann and others, 2018) and Lemon Creek (Veitch and others, 2021) Glaciers in Alaska. Active-source seismic methods are also able to resolve englacial heterogeneity in elastic properties where recorded frequencies are sufficiently high. Examples include mapping a 40 m deep englacial conduit at Rhonegletscher with a dominant frequency of 100 Hz (Church and others, 2019), mapping debris layers at Sourdough rock glacier in Alaska (Kuehn and others, 2024) with a 100 Hz dominant frequency, and building a seismic-velocity profile through the upper 80 m of firn at Korff Ice Rise in West Antarctica using a dominant frequency of 200 Hz (Agnew and others, 2023).

Typically, a two-dimensional (2-D) seismic survey is sufficient for estimating elastic velocities from which bedrock topography and ice thickness, h, can be calculated. When source-receiver offset distances are long relative to the bedrock depth (i.e., $> 3\times$), refracted P-wave energy can be used to constrain P-wave velocity models (V_p) at depth (e.g., Redpath, 1973). For more limited-offset surveys, Rayleigh waves that propagate along the surface of the Earth and are strong reliable signals (e.g., Socco and Strobbia, 2004) can be used to constrain S-wave velocity (V_s) depth profiles (Crice, 2005). Active-source experiments on glaciers are often offset-limited due to the logistical challenges of operating on ice (Aster and Winberry, 2017), which suggests that Rayleigh wave methods should be well suited for glacial experiments.

There are two common approaches for deriving elastic model properties from Rayleigh waves: (1) the horizontal-vertical spectral ratio (HVSR) method, which exploits the elliptical particle motion of this wave; and (2) the multi-channel analysis of surface waves (MASW), which exploits the dispersive nature of the wave (i.e., the change in wave propagation velocity with frequency).

The HVSR approach calculates h from the resonant frequency (f_0) of ambient Rayleigh-wave energy recorded on a seismic array in conjunction with a V_s estimates that is typically derived from P-waves recorded on a co-located active-seismic survey and an empirical V_p/V_s ratio. We refer the reader to Picotti and others (2017) and Preiswerk and others (2019) for seminal applications of HVSR in glacier settings. Stevens and others (2023), for example, applied this workflow to a combined dataset acquired on the Saskatchewan Glacier in the Canadian Rocky Mountains, using an "accepted" $V_p/V_s = 1.95$.

The HVSR method assumes a layer-over-half-space model from which the upper layer thickness, h, can be estimated as $h = \frac{V_s}{4f_0}$ (Ibs-von Seht and Wohlenberg, 1999). The HVSR method has caveats that limit its applicability in complex environments like those found in firn-aquifer systems. In these settings, HVSR's core assumptions — lateral homogeneity and the validity of h estimates based on a layer-over-half-space system (Koller and others, 2004) — are often violated. This underscores the need for applying alternative velocity model-building approaches that explicitly avoid homogeneity assumptions and reduce or eliminate the need for empirical relationships.

MASW is one such velocity modeling approach which avoids uncertainties arising from the homogeneity assumptions of the HVSR method and exploits Rayleigh-wave dispersion in layered medium. Developed by Park and others (1999), MASW is widely used in geotechnical engineering (e.g., Crice, 2005) where dispersion caused by near-surface layering is expressed as the change in Rayleigh-wave phase velocity V_r as a function of frequency f (and consequently depth, z). As opposed to HVSR, MASW is commonly implemented on low-energy, active-source experiments and analyzes higher frequency surface waves with shallower penetration depths. At Sourdough Rock Glacier, Alaska, Kuehn and others (2024) employed 12 vertical-component (1-C) geophones at 5 m spacing and generated accurate seismic velocity estimates of the upper 5 m of the ice column. At Spitsbergen in the Norwegian Arctic, the MASW method was used to constrain meltwater at a deeper ice-bed interface (down to 200 m) by inverting multi-mode dispersion curves (Tsuji and others, 2012). This required a longer receiver array (1500 m) in which they used 60 1-C geophones deployed at 25 m spacing.

MASW is a relatively straightforward workflow, made accessible through open-source software such as *MASWaves* (Olafsdottir and others, 2018b). However, it demands careful implementation and interpretation of inversion schemes and results due to the inherent non-uniqueness of solutions (Foti and others, 2018). In glacial settings, the ill-posed nature of the inverse problem is further amplified by logistical surveying constraints, such as being limited to a small number of receivers or low-impact sources in weight-limited field expedition. This has motivated some practitioners to implement more advanced inversion approaches, such as the transdimensional Bayesian inversion applied at Helheim Glacier, Greenland (Killingbeck and others, 2020).

In this study, we aim to address the ill-posedness of MASW for the typical limited-aperture receiver arrays in glaciological applications by exploring how optimized survey design, enhanced data preconditioning, and the use of three-component (3-C) instruments can reduce observational uncertainty and thereby improve the effective depth of investigation. We begin with an overview of Rayleigh-wave theory relevant to MASW, followed by three synthetic studies that each examine sensitivities of MASW to data conditioning, acquisition geometry, and subsurface complexity. In all case studies, we simulate and analyze multi-component (MC) datasets and develop an MC-MASW approach which accounts for their complementary contributions. Finally, we apply MC-MASW to an aperture-limited dataset acquired on the Saskatchewan Glacier in the Canadian Rocky Mountains (Stevens and others, 2023). We conclude by offering key recommendations for MC data acquisition, preprocessing, and Rayleigh-wave dispersion analysis in glacial investigations.

THEORY

This section reviews Rayleigh wave theory using potential wavefields (P- and S-waves) rather than the displacement wavefields commonly presented in textbooks. Although displacement-based formulations are widely used for their practical application in matrix methods for solving the wave equation (Aki and Richards, 2002), our approach follows Lay and Wallace (1995) and provides insight into the underlying principles of our MC approach to Rayleigh wave analysis.

Assumptions and notation

We focus on the 2-D problem in the x–z plane of wave propagation, restricting the development to isotropic, linear elastic solids. Extending these studies to account for anisotropy is a natural progression of this work, particularly given that ice is generally considered anisotropic. We assume an acquisition field coordinate system in which the vertical z and horizontal x directions are positive downward and to the right, respectively (Fig. 1a). Wavefield displacements in the z and x directions are respectively denoted U_z and U_x. Without loss of generality, we assume that the free-surface interface occurs at $U_z = 0$ m.

Horizontal-component geophone data are rotated into a cylindrical coordinate system centered about the source point with horizontal radial-transverse (R–T) components to isolate the azimuthal dependence of recorded particle displacement. The R and T components for any source-receiver pair respectively point along and perpendicular to the source-to-receiver azimuth (Fig. 1b). Here, we limit our analysis to R-component data.

A complete list of abbreviations and symbols used in this paper is provided in Appendix A and Appendix B, respectively.

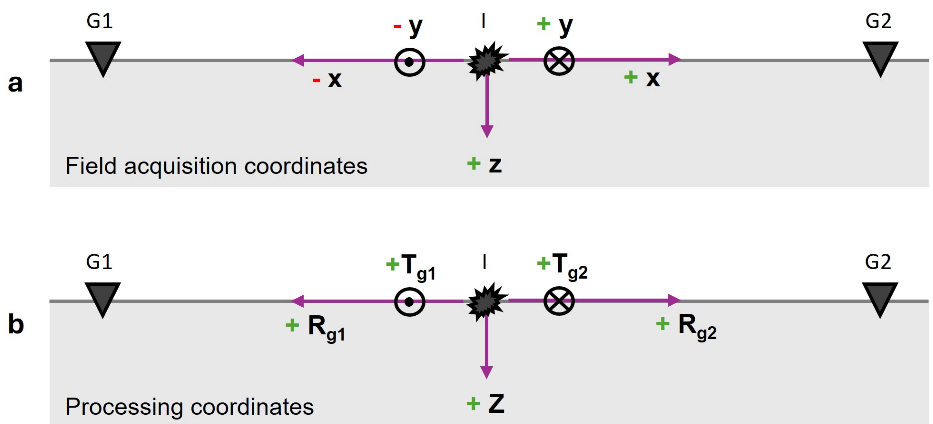

Fig. 1. Definition of the (a) acquisition coordinate system in horizontal x and y and vertical z directions, and (b) the cylindrical processing coordinate system in outward-positive radial R and vertical Z directions. The transverse, T direction is always counter clockwise from R. I and G annotate the locations of the impact source and receivers in each sketch.

Rayleigh waves

Rayleigh waves exist in the near surface of an elastic medium due to the interference of elastic body waves (specifically, the P-SV wave system with S-wave particle motion polarized in the plane of wave propagation) and their conversions at the free surface (here, the air-ice interface) (Lay and Wallace, 1995; Liner, 2012). These two wave modes are coupled: when either wave interacts with a boundary with discontinuous material properties, the resulting reflection, refraction, and transmission effects occur in addition to wave-mode conversion (Fig. 2a). Fig. 2b illustrates this mechanism for an incident reflected PS wave striking the free surface at an angle j. Interaction of this wave mode with the free surface produces a twice-converted P wave (PSP) and a converted SV wave (PSS), that are respectively reflected at angles j and i and propagate with velocities V_p and V_s of the first layer. Rayleigh waves are generated when the SV wave meets the free surface where surface tractions vanish at (and beyond) a critical angle. The incident SV wave is converted into a refracted P wave (propagating along the surface) and a 180° phase-shifted, post-critical reflection of

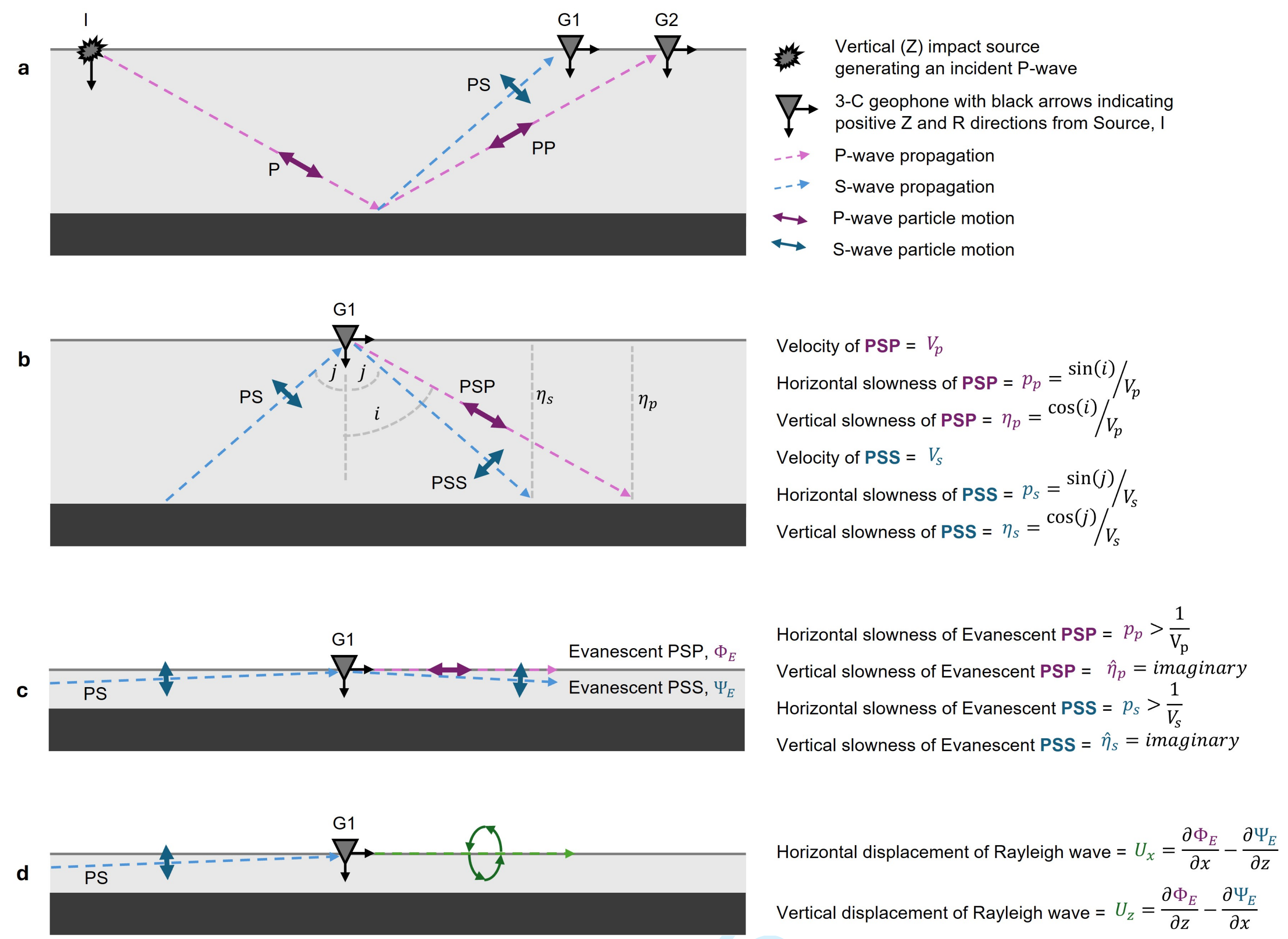

Fig. 2. Conceptual representation of Rayleigh-wave generation from a vertical impact source I. (a) An incident P wave reflects off an impedance contrast producing up-going reflected P (PP) and S (PS) waves. (b) The up-going PS wave undergoes total internal reflection at the free surface producing a PSS wave and a mode-converted PSP wave. The velocity and horizontal and vertical slownesses are described relative to the free-surface incidence angle. (c) At large angles of incidence, evanescent PSP and PSS waves propagate along the surface out-of-phase thus producing (d) a Rayleigh wave with retrograde elliptical particle motion along the free surface. U_z and U_x are described in terms of the potentials, Φ and Ψ, of the evanescent wavefields.

SV wave energy (with near-vertical particle motion that grazes the surface) (Lay and Wallace, 1995). The respective wave-mode interactions with the free surface generate evanescent P- and SV-waves (Fig. 2c). The resulting P- and SV-wave displacements are described by the gradient of the scalar potential, Φ, and the curl of the vector potential, Ψ, respectively.

The simultaneous existence of these two out-of-phase modes generates a Rayleigh wave with elliptical particle motion (Lay and Wallace, 1995) that propagates along the surface (Fig. 2d). Rayleigh-wave vertical (U_z) and horizontal (U_x) displacements are represented by sums of spatial derivatives of Φ_E and Ψ_E. For a homogeneous Earth system, the equations associated with Fig. 2d are expanded as:

$$U_x = -A\omega p \sin\left(\omega(px - t)\right)\left[\mathrm{e}^{-\omega\hat{\eta}_p z} + \frac{1}{2}\left(\frac{{V_r}^2}{V_s^2} - 2\right)\mathrm{e}^{-\omega\hat{\eta}_s z}\right], \tag{1}$$

and

$$U_z = -A\omega p \cos\left(\omega(px - t)\right)\left[V_r\hat{\eta}_p\mathrm{e}^{-\omega\hat{\eta}_p z} + \frac{1}{V_r\hat{\eta}_s}\frac{1}{2}\left(\frac{{V_r}^2}{V_s^2} - 2\right)\mathrm{e}^{-\omega\hat{\eta}_s z}\right]. \tag{2}$$

The displacements are a product of three terms: (1) amplitude terms dependent on the angular frequency ω, the horizontal slowness p of the Rayleigh wave, and a scaling constant A; (2) time-dependent terms describing harmonic plane-wave motion along the x direction; and (3) terms specifying amplitude decay with depth z dependent on vertical slownesses $\hat{\eta}_p$ and $\hat{\eta}_s$ defined by

$$\hat{\eta}_p = \sqrt{\frac{1}{V_r^2} - \frac{1}{V_p^2}} \tag{3}$$

and

$$\hat{\eta}_s = \sqrt{\frac{1}{V_r^2} - \frac{1}{V_s^2}}. \tag{4}$$

The time-dependent terms are described by orthogonal *sine* and *cosine* functions that produce elliptical particle motion because of generally larger displacements in U_z compared to U_x. At the free surface, the sense of elliptical particle motion is retrograde; however, this changes to prograde at depth h_r where the third term of Equation (2) becomes zero causing $U_x = 0$. The depth h_r can be analytically calculated as

$$h_r = \frac{\ln\left(1 - \frac{V_r^2}{2V_s^2}\right)}{\omega\left(\hat{\eta}_s - \hat{\eta}_p\right)}, \tag{5}$$

or approximated based on the dominant wavelength (Ammon and others, 2020), $\lambda = V_r/f$, as

$$h_r \approx \frac{1}{5}\lambda. \tag{6}$$

To validate that this general expression holds for glacial ice, we compare equations (5) and (6) for three models (Fig. 3) — a saturated soil profile (Yang, 2005), a Poisson solid (Ammon and others, 2020), and glacial ice referenced from Saskatchewan Glacier (Stevens and others, 2023). The velocities of each model are listed in rows a, b and c1 in Table 1. The similarity between the true and approximate solutions suggests that Eqn. (6) is a reasonable estimate for the three tested models.

Table 1. Elastic properties for different subsurface media examined in our analytical models: a. fully saturated soil profile (Yang, 2005); b. Poisson solid (Ammon and others, 2020); c1. ice layer derived from the Saskatchewan Glacier (Stevens and others, 2023); c2. ice layer derived from the Greenland Ice Sheet (Walter and others, 2015); c3. ice layer derived from Nathorst Land, Spitsbergen (Johansen and others, 2011); d. firn layer derived from the Helheim Glacier, Greenland (Killingbeck and others, 2020). Note that although some case studies report higher-precision values, we have rounded results to the nearest hundredth for consistency.

	Model	V_p (m s^{-1})	V_p/V_s	V_r/V_s
a	Fully Saturated Soil	1550	6.30	0.95
b	Poisson Solid	5800	1.73	0.92
c1	Ice (Saskatchewan Glacier)	3450	1.95	0.93
c2	Ice (Greenland Ice Sheet)	3870	2.10	—
c3	Ice (Spitsbergen)	3600	2.00	—
d	Firn (Helheim Glacier)	2900	2.23	—

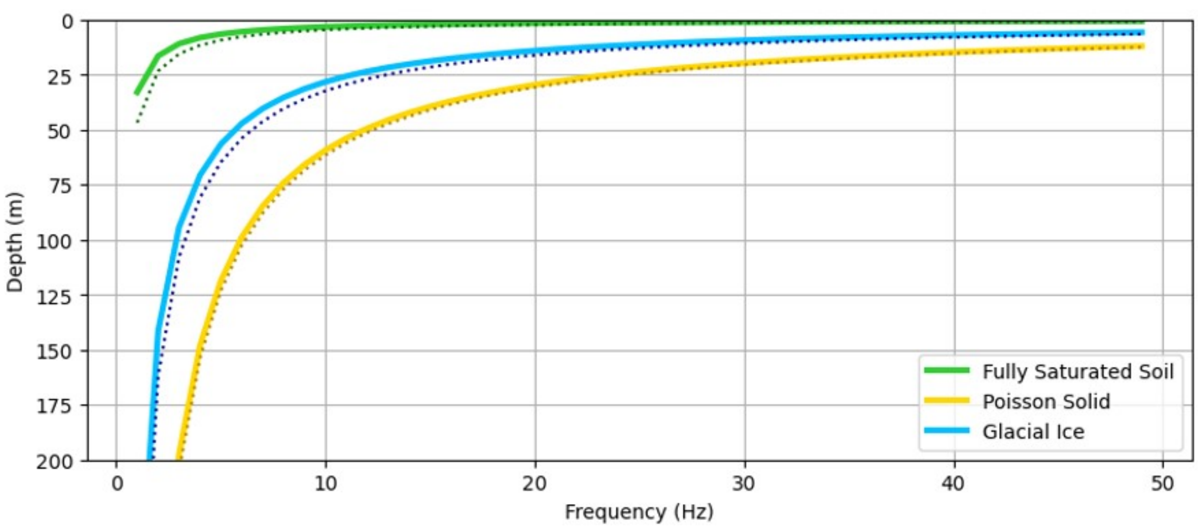

Fig. 3. Frequency-dependent depths at which Rayleigh-wave particle motion change from retrograde to prograde for a fully saturated soil profile (green) (Yang, 2005), a Poisson's solid (yellow) (Ammon and others, 2020), and glacial ice (blue) based on parameters estimated for the Saskatchewan Glacier (Stevens and others, 2023). Solid line are analytical solutions (Eqn. (5)), and dotted lines are approximated depths (Eqn. (6)) for all models. Table 1 lists associated material properties.

The depth-dependent terms are eigenfunctions for which the Rayleigh-wave phase velocity V_r is the eigenvalue (Aki and Richards, 2002). This is an important feature, as it provides a means of solving for V_r using the characteristic equation derived from the eigenproblem. For the homogeneous half-space model, the characteristic equation simplifies to

$$\frac{V_r^6}{V_s^6} - 8\frac{V_r^4}{V_s^4} + \left(24 - 16\frac{V_s^2}{V_p^2}\right)\frac{V_r^2}{V_s^2} + 16\left(\frac{V_s^2}{V_p^2} - 1\right) = 0. \tag{7}$$

We refer the reader to Ammon and others (2020) for a digestible derivation of this equation starting from the potential field definitions of the stress tensor at the free surface. Note that Eqn. (7) is a cubic polynomial in V_r^2/V_s^2 and that solutions for V_r are highly sensitive to V_s, a fact that provides an opportunity to derive a $V_s(z)$ profile from the Rayleigh-wave data via inversion. Although there are multiple solutions for V_r, the solution is constrained by realistic V_p/V_s ratios. We visualize this constraint by plotting V_r/V_s versus V_p/V_s (Fig. 4) and note the solution for a Poisson solid, fully saturated soil and several glacial estimates (Table 1) derived from published studies. Fig. 4 suggests that glacial estimates of V_r/V_s are slightly higher than that of a Poisson solid.

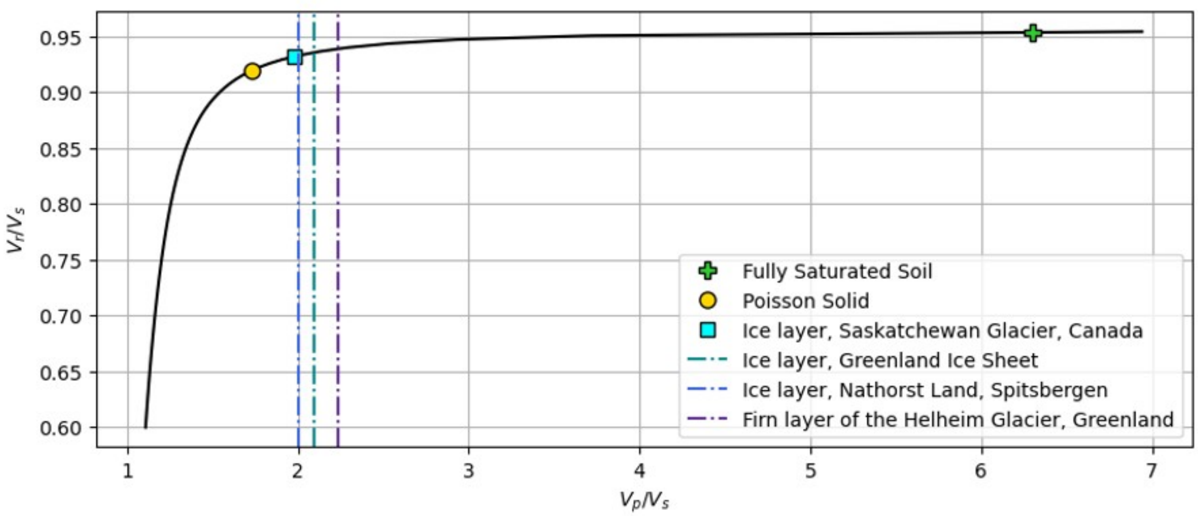

Fig. 4. Rayleigh-wave characteristic equation (Eqn. (7)) represented as a relationship between V_p/V_s and V_r/V_s (black curve) with reference values for a saturated soil (green cross), Poisson solid (yellow circle), and glacial ice at the Saskatchewan Glacier (cyan square). V_p/V_s estimates of other glacial examples are plotted as vertical lines since V_r/V_s estimates are not mentioned in reference studies. Table 1 lists associated material properties.

Layering and dispersion effects

In a layered Earth, the Rayleigh-wave displacement and characteristic equations become more complex due to the introduction of a relationship between V_r and f. In an Earth model where velocities generally increase with depth, lower-frequency wave modes propagate deeper, interacting with faster velocities, and therefore arrive earlier than the higher-frequency modes. This velocity-dependence on frequency (i.e.,

$V_r(f)$) is called dispersion. We refer the reader to Ammon and others (2020) for a comprehensive physical overview of dispersion phenomenon and to Aki and Richards (2002) for more advanced mathematical treatment. Whereas equations (1) and (2) may be solved analytically for a homogeneous Earth model, Rayleigh-wave displacements and dispersion need to be calculated numerically for general layered Earth scenarios (Aki and Richards, 2002).

Each frequency in a propagating Rayleigh wave carries velocity information about a range of depths with variable sensitivity. At the high-frequency limit, λ is potentially much shorter than the thickness of the uppermost layer. That is, the wave displacement is entirely contained within that single layer and the effective velocity of this high-frequency component of the Rayleigh wave is dominantly controlled by properties of the uppermost layer. At longer wavelengths, the wave interacts with multiple layers at any given time and thus mapping V_r to a specific depth requires untangling the overlapping frequency-dependent sensitivities of Rayleigh-wave displacement to different depths.

Short of calculating velocity-dependent sensitivity kernels of the eigenfunctions, a reasonable assumption is that the Rayleigh-wave depth of investigation, h, is equal to a half wavelength, $\lambda/2$ (Park and others, 1999). The minimum and maximum depths of investigation, respectively denoted h_{min} and h_{max}, are given by

$$h_{min} \approx \frac{\lambda_{min}}{2} \approx \frac{V_{r,min}}{2f_{max}} \approx \Delta r_x \tag{8}$$

and

$$h_{max} \approx \frac{\lambda_{max}}{2} \approx \frac{V_{r,max}}{2f_{min}} \approx \frac{L}{3} \text{ to } \frac{L}{2}, \tag{9}$$

where receiver spacing Δr_x and array length L control the shortest and longest wavelengths, λ_{min} and λ_{max}, measurable on an array. The recoverable wavelengths are themselves constrained by the Nyquist sampling theorem (Socco and Strobbia, 2004; de Lucena and Taioli, 2014).

Subsurface layering can act as waveguides that increase propagating wavefield complexity. As waves reflect and refract within these layers, only certain frequencies will align in a manner that produces coherent, stable oscillations, which manifest as higher-order modes. The limiting frequencies over which a higher-order mode exists are a function of layer thickness, depth, velocity contrasts, and propagating frequencies. The modes are distinguishable by their different dispersive behavior and dominant frequency ranges. Higher-order modes are particularly important for recovering complex models with velocity inversions (i.e., where a fast velocity material overlies a slow velocity medium). A low-velocity layer will bend the transmitted ray toward the normal and allow for high-frequency oscillations within this layer. Multi-mode analysis can be necessary for characterizing voids or unfrozen layers (e.g., at Spitsbergen in the Norwegian Arctic; Tsuji and others, 2012) or firn-aquifer systems (e.g., at the Helheim Glacier in Greenland; Killingbeck and others, 2018).

In a layer-over-half-space model, fundamental mode amplitudes are strongest. In layered media, the fundamental mode is strongest at lower frequency ranges (with the exact range dependent on layer thickness and velocities) and thus controls the maximum depth of investigation. Our investigations focus on fundamental-mode dispersion, although including higher-order modes would be a natural progression of this work.

METHODS AND IMPLEMENTATION

MASW dispersion analysis

MASW dispersion analysis hinges on generating plots showing relative signal amplitude in $V_r - f$ space, commonly referred to as dispersion panels (DPs), in order to estimate V_r of the fundamental mode as a function f, or the dispersion curve (DC). To construct DPs for dispersion analysis, the seismic data are first organized into shotgathers of the form $D(d, t)$, where d represents the offset and t the recording time. Each gather contains all time-series traces recorded from a single shot, sorted by increasing offset. Each shot gather is then transformed to the frequency domain ($D(d, \omega)$) and subsequently normalized ($D_N(d, \omega)$) in both the offset and frequency dimensions (Park and others, 1998) to minimize the influence of geometrical spreading and attenuation effects. The normalized amplitudes at each offset and frequency ideally are representative of dispersion effects. Through slant-stack processing (Olafsdottir and others, 2018b), traces are move-out corrected, stacked, and normalized by the number of traces for a user-selected range of phase velocities and frequencies producing DPs ($D_S(V_r, \omega)$). DCs are picked along the (ideally continuous) peak-magnitude trend. We used the open-source *MASWaves* software package (Olafsdottir and others, 2018b) to generate DPs and automatically pick DCs based on maximum amplitude.

A comprehensive analysis of surface-wave dispersion typically involves inverting these DCs to obtain V_s depth profiles which inform interpretations of subsurface structure and mechanical behavior. However, we focus on improbving the forward problem by constructing accurate and reliable DCs that are an essential yet underexplored aspect in the MASW literature — especially in the context of cryospheric field experiments.

Design of DC sensitivity studies

The inversion of surface-wave dispersion data is a strongly ill-posed problem, largely due to the complex wave physics involved — complexities we have simplified in the above Theory section. As a result, the accurate extraction of DCs becomes critically important, particularly in glaciated environments where surveys are often constrained by limited array lengths, low receiver counts, shallow source penetration, and non-ideal (near-)surface conditions, such as crevassing. To systematically investigate these limitations, we design three synthetic studies.

The first simulates an ideal active-source survey, which features a long array and dense spatial sampling, over a simple two-layer model to establish best-practice data conditioning steps. The second study uses the same model but applies non-ideal survey designs to explore how acquisition geometry alone can limit the forward problem, even under optimal conditioning. In the third study, we simulate wave propagation through three variations of firn-aquifer models to test the robustness of our conditioning approach under more realistic near-surface complexity. All studies examine MC datasets, using both vertical (Z) and radial (R) component data. In the final study, we also develop an approach for integrating these components in an MC-MASW framework that enhances DC accuracy with minimal changes to field deployment or processing workflows.

The synthetic MC data were simulated with the open-source SOFI2D seismic modeling package (Bohlen and others, 2016). For all experiments, a vertical impact source was simulated as an Ormsby wavelet with a flat frequency spectrum between 5 Hz and 30 Hz. For all studies, sources and receivers were positioned 1 m below the free surface. Because individual simulations had only positive offsets ($d > 0$), the horizontal-component data correspond to the radial R component for all source-receiver pairs. For field studies with non-uniform geophone orientation and for multi-azimuth acquisitions with directional (signed) offsets, rotating recorded data into a $R - T$ coordinate system would be a critical data preprocessing step.

Field data implementation

Building on the data conditioning strategies and multi-component (MC) analysis developed through the synthetic studies, we apply MC-MASW to a field dataset acquired on Saskatchewan Glacier (Stevens and others, 2023, 2024). The raw 3-C field data were organized into shot-gathers using *ObsPy* (Beyreuther and others, 2010). Although the horizontal components were predominantly parallel and orthogonal to the 2-D array axis we applied an $R - T$ rotation to correct for any minor misalignment. This rotation and other minor data refinement (e.g. time-shifts and noise filtering) were completed using the open-source *Seismic Unix* seismic processing software package (Stockwell Jr, 1999).

Unlike the controlled synthetic scenarios, the field data presented additional challenges due to ambient noise and other sources of variability. To address this, we implement supergather processing (e.g., Shragge and others, 2021), which combines multiple shot gathers and not only improves DC reliability but also enhances depth sensitivity of the MASW analysis. This is detailed in the presentation of results.

RESULTS: DC SENSITIVITY STUDIES

In this section, we present the results of three synthetic feasibility studies designed to assess DC sensitivity of MC data to data conditioning, acquisition geometry, and subsurface complexity. Each study isolates key factors that affect the accuracy and reliability of the forward problem in MC-MASW analysis.

Study 1: DC Sensitivity to Data Conditioning

We used a two-layer, isotropic elastic 2-D model to numerically simulate MC data under ideal survey conditions (Fig. 5). The goal was to identify data conditioning steps that enhance DP resolution and improve the accuracy of extracted DCs. The model consisted of a homogeneous ice layer overlying a bedrock half-space, representative of conditions commonly found in the ablation zone of mountain glaciers. The material properties used in this model are summarized in Table 2 and are adapted from Stevens and others (2023)'s study at Saskatchewan Glacier.

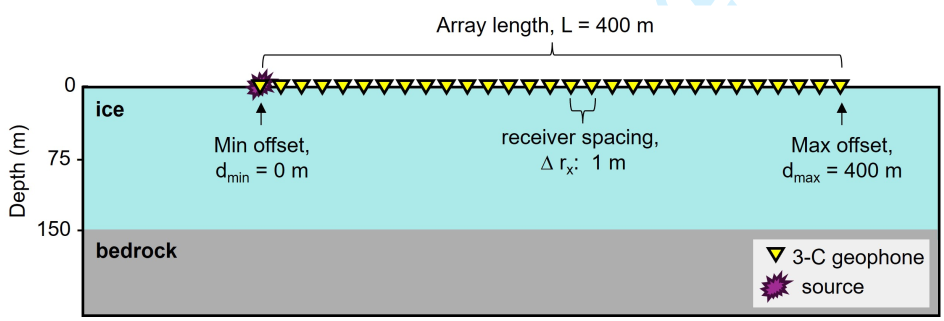

Fig. 5. Model describing a homogeneous, isotropic, elastic ice layer of 150 m thickness overlying a bedrock half space. Table 2 presents the elastic model properties. The idealized acquisition has a dense 1 m receiver spacing and 400 m aperture. The sketched geometry is not to scale and approximates receiver placement for visual reference.

Fig. 6 presents a representative example of the Z- and R-component synthetic data. The shot gathers (Fig. 6a, 6c) exhibit a strong Rayleigh-wave arrival with linear moveout (i.e., arrival time linearly increasing with offset d), and the direct P-wave arrival has higher raw amplitudes on the R component in comparison to

Table 2. Two-layer homogeneous ice-bedrock model elastic properties (Stevens and others, 2023)

Layer	V_p (m s^{-1})	V_s (m s^{-1})	Density (ρ) (kg m^{-3})	Thickness (h) (m)
Ice	3500	1750	930	150
Bedrock	4000	2000	2600	∞

those observed on the Z component. Using *MASWaves*, the shot gathers and relevant acquisition geometries (i.e., d_{min}, Δr_x, number of traces and orientation of offsets) were input to create DPs (Fig. 6b, 6d). Z- and R-component DCs are automatically picked using the *MASWaves* algorithm at increments of 1 m s^{-1} for frequencies between 6 and 40 Hz.

Given the known elastic model parameters and frequency range of interest, we calculated and plotted the numerical solutions for the fundamental (black line) mode using the open-source *Disba* software package (Luu, 2021). Additionally, provided that the depth of investigation is related to V_r and f through Eqn. (9), we plot maximum wavelengths (red dashed lines) for resolving depths of 200 m (in bedrock), 150 m (ice-bedrock interface) and 20 m (in ice). Picked DCs at frequencies to the left of these depth-resolving relationships are unreliable. To the right of these lines, the depth-sensitivity of each frequency band varies according to the displacement eigenfunctions associated with the layered equivalent of equations (1) and (2). Eqn. (9) also presents an approximation of the maximum depth of investigation based on array length. Given $L = 400$ m, we estimate $h_{max} = 133$ to 200 m which aligns with the low-frequency limit of observable strong amplitudes on the DPs (Fig. 6b and 6d).

For this synthetic model, the physics as implemented in the numerical solutions show that there is no observable dispersion at higher frequencies (over approximately 10 Hz) due to the homogeneity of the shallow ice layer. Above 20 Hz, the numerical solution of the fundamental mode (black line) is constant at 1670 m s^{-1} whereas the picked DC (herein referred to as experimental DC) averaged from the Z and R components is 1630 m s^{-1} with a 10 m s^{-1} discrepancy between the components.

The ice-bedrock layering generates dispersion in the $5 - 10$ Hz frequency band indicative by the slope of the numerical solution. The DPs, though, are more complicated than theory suggests. Below 20 Hz, the resolution of the DPs declines as the high-amplitude band broadens and loses definition. Additionally at even lower frequencies (below approximately 10 Hz), the Z- and R-component trends deviate from each other and the true solution. At 10 Hz, the difference between the experimental Z and R DCs is 180 m s^{-1} (>10% of the signal).

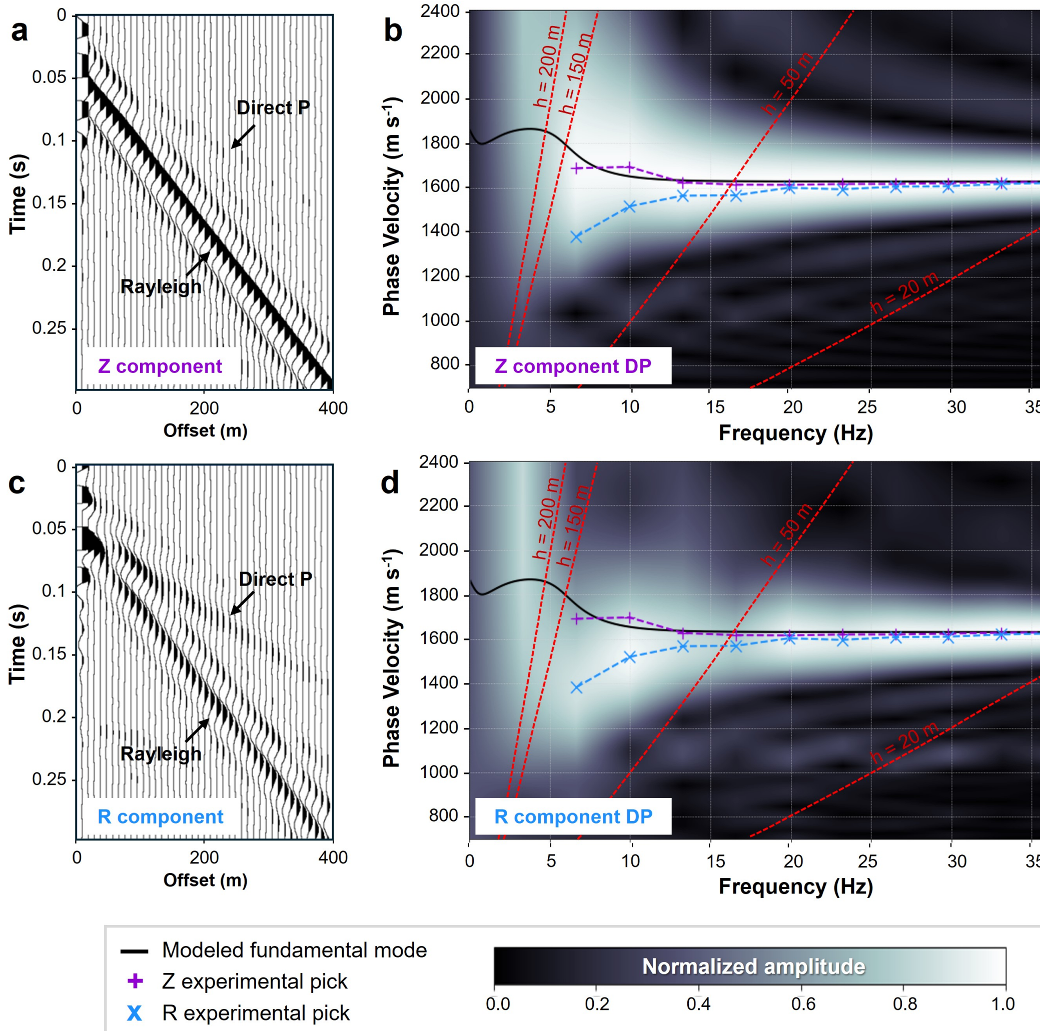

Fig. 6. (a) Raw Z-component shot-gather data with corresponding (b) Z-component and (c) raw R-component shot-gather data with corresponding (d) R-component DP for the two-layer ice-bedrock model (Fig. 5), with the numerically calculated DC for the fundamental model (black line). Every 10th trace is shown in the shot gathers for display purposes. Dashed red lines on DPs highlight the maximum wavelengths for resolving depths 20 m, 150 m, and 200 m; valid regions for picking experimental DCs for each depth range fall to the right of these lines. The experimental DCs for the Z- (purple) and R- (blue) components are displayed on both DPs. We note the DC complexity particularly for R and sub-10 Hz Z, which are not consistent with the numerical solution.

The numerical solutions are the vector-oriented solutions, i.e., they assume that particle displacement is calculated tangentially to the elliptical particle motion. To investigate whether and why the Z- and R-component dispersion trends differ, we examine depth-sensitivity of the eigenfunction, herein referred to as sensitivity kernels. In Fig. 7, we compare $U_z(z)$ and $U_x(z)$ for the fundamental mode at discrete frequencies in the $5 - 40$ Hz band. Elliptical retrograde particle motion occurs where $U_x < 0$, $U_z > 0$, and $|U_z| > |U_x|$, then transitions to a prograde motion at depth. These depths can be identified by the R component data where $U_x = 0$; solid arrows on Fig. 7 highlight these depths for the discrete frequencies.

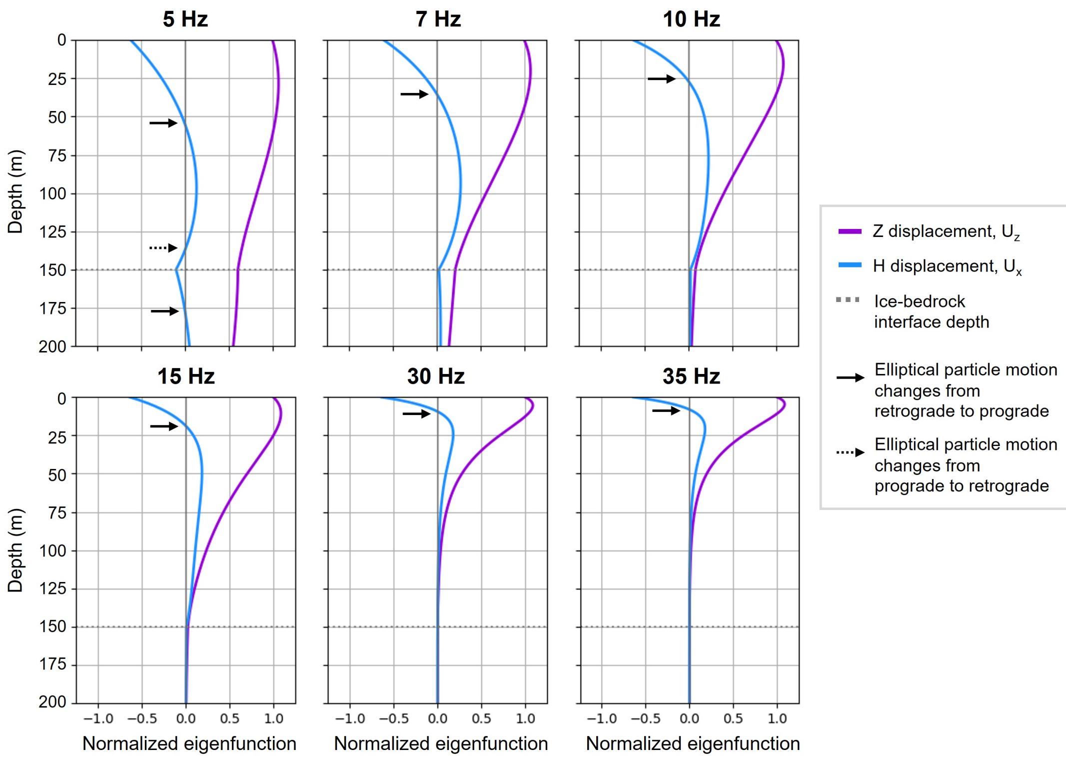

Fig. 7. Monochromatic depth-sensitivity kernels for the two-layer homogeneous-ice model (Fig. 5). Curves are the eigenfunctions (the layered-model equivalent of the third terms of equations (1) and (2) normalized to $U_z(Z = 0) = 1$) and represent the sensitivity of U_z (purple) and U_x (blue) components to discrete model depths and wave frequencies. The dotted gray lines show the ice-bedrock interface depth for which only the $5 - 10$ Hz panels show non-zero U_z sensitivity and only $5 - 7$ Hz show non-zero U_x sensitivity.

The lowest frequency ($5 - 10$ Hz) components are most sensitive to the ice-bedrock interface at 150 m (dotted gray line). Above 10 Hz, the null Z- and R-component displacement at these depths indicate that the higher-frequency Rayleigh waves carry no information about the bedrock layer. Thus measuring dispersion at sub-10 Hz frequencies are critical for characterizing bedrock properties for this ice thickness.

There are two additional features of the 5 Hz U_x sensitivity kernel that provide important observational constraints on the system: (1) the second and third reversals in the sense of rotation at 130 and 175 m; and (2) an inflection point on U_x that occurs at the ice-bedrock interface (also observed with a smaller amplitude at 7 Hz). Our later analysis of a multi-layered system explores these observations in detail.

Effective data conditioning is crucial for constructing broadband, high-resolution DPs and facilitating accurate DC picks. Although data preprocessing is not always straightforward, two guiding principles apply for MASW purposes: (1) isolating the Rayleigh-wave mode; and (2) ensuring that each trace in the selected shot-gather window contains untruncated dispersive Rayleigh-wave energy. Furthermore, any noise-reduction effort applied to the MASW data input likely will improve experimental pick accuracy.

Below 20 Hz, R-component data are strongly affected by the direct P-wave arrival traveling sub-horizontally near the surface at 3500 m s^{-1}. We capture these arrivals in the shot gather (Fig. 6c), and they cause substantial sub-20 Hz distortion of the corresponding DP (Fig. 6d). Fig. 8 shows the same data, but after removing the direct wave through frequency-wavenumber dip filtering. This filtering step improves DC generation for both Z- and R-components: at 10 Hz, the mean difference between experimental Z- and R-component picks (Fig. 8d) is reduced from 180 m s^{-1} to 40 m s^{-1}, while the mean difference between the experimental picks and numerical solution is now reduced from 130 m s^{-1} to 60 m s^{-1}.

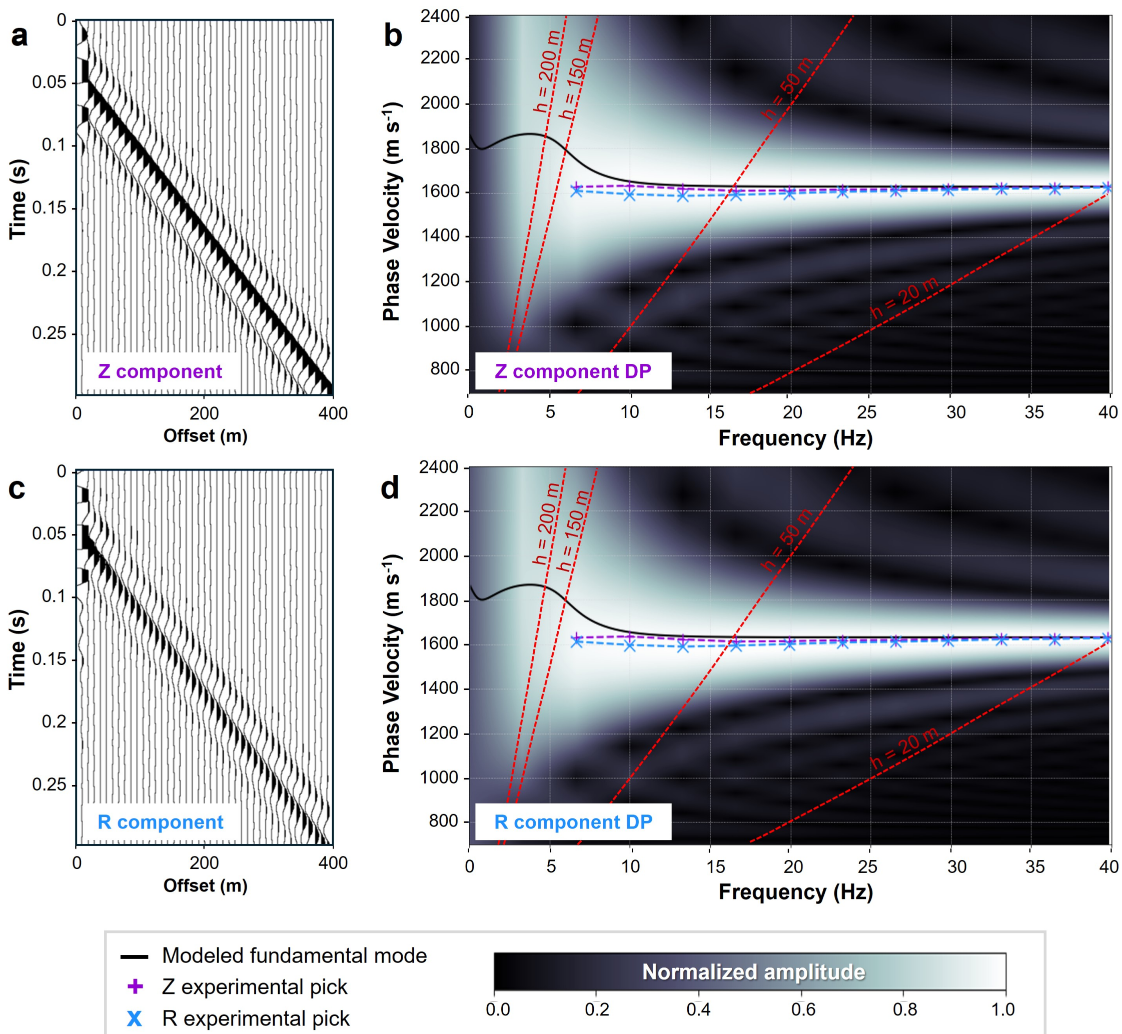

Fig. 8. Conditioned shot gathers and DPs after removing the direct P-wave arrivals. See Fig. 6 for descriptions of individual panels. Note the substantial improvement in the continuity of the R-component DPs, with the mean Z- and R-component pick discrepancy reduced from 180 m s^{-1} to 40 m s^{-1}. Additionally, the experimental Z- and R-component picks are more closely aligned to the numerical solution (black line) — reduced from 130 m s^{-1} to 60 m s^{-1}.

In field experiments, it is common practice to position a zero-offset ($d = 0$ m) receiver nearby the shot point to record time zero. This is critical information for windowing continuous geophone records into shot gathers. However, zero-offset data are often more complex close to the source point and, if used, can degrade dispersion curves. Ideally, shot-gather data should be windowed such that the full Rayleigh wavefield (including all possible dispersive effects) fall within the window selected to generate the DPs. Fig. 9 shows the shot gather from Fig. 8 after removing the near-offset traces (i.e., $d < 10$ m) and adjusting the panel window times to capture the full wavelet at all offsets.

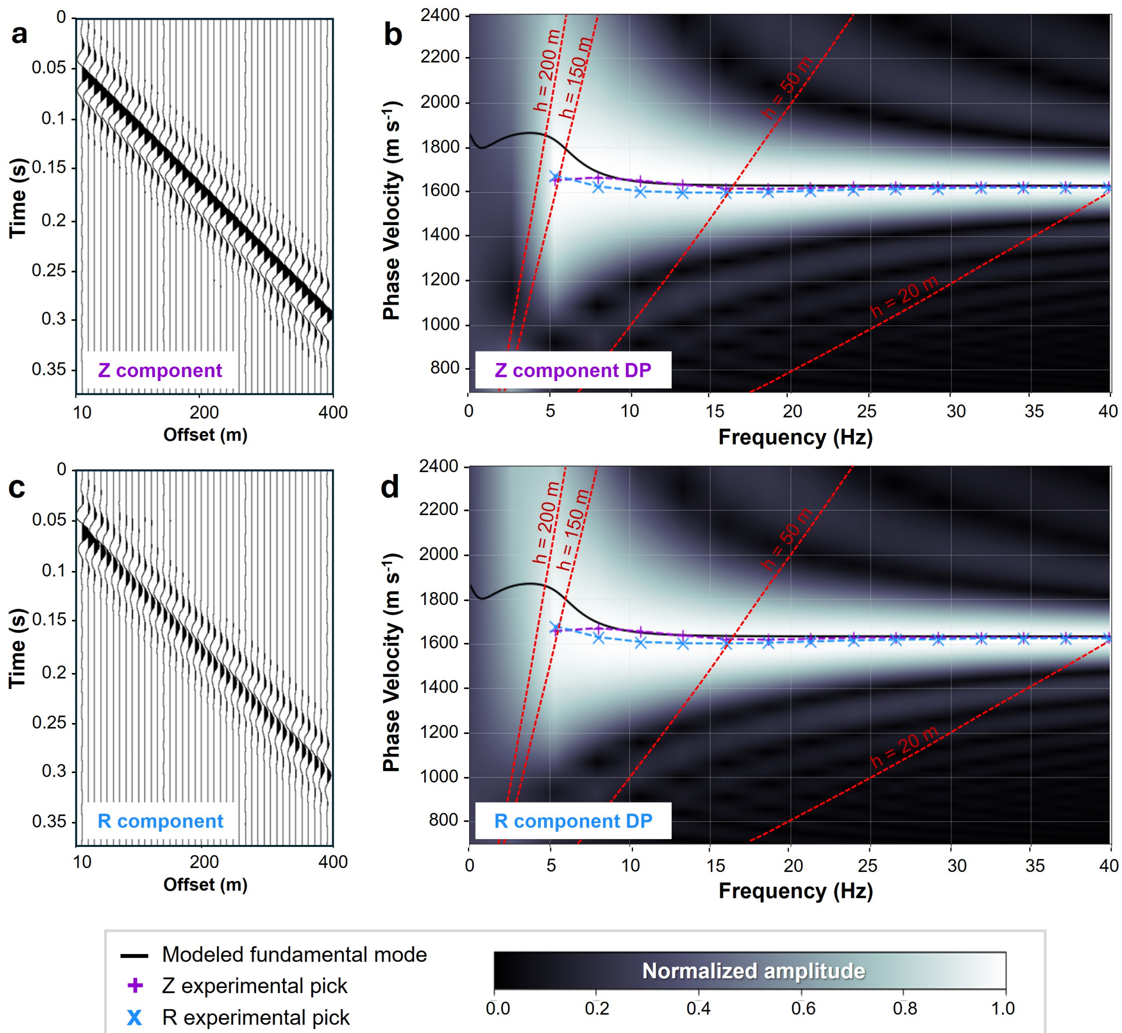

Fig. 9. Conditioned shot gather data and DPs after removing the direct P-wave arrival and windowing out noisy near-offset traces to highlight the full Rayleigh-wave character at far offsets. See Fig. 6 for descriptions of individual panels. We improved sub-10 Hz resolution of the DPs with appropriate data conditioning.

At 10 Hz, the discrepancy between experimental Z- and R-component picks and the mean difference between the experimental picks and the numerical solution are similar to the prior stage of removing the direct wave (Fig. 9). However, the substantial value of this conditioning step is in improving DP resolution (i.e., stronger and more localized magnitudes). Below 5 Hz, the DP is abruptly truncated, which is accurate given that the Ormsby source wavelet used for simulation lacks frequencies below 5 Hz.

Study 2: DC Sensitivity to Acquisition Geometry

Practical limitations on survey design are often a restricting factor in geophysical field experiments. For example, active seismic experiments require transportation of a source (typically a sledgehammer), a base plate, and numerous geophones, and involve careful geophone deployment to ensure sufficient coupling and accurate positioning and potentially orientation, all of which can be challenging in glacial field conditions (Aster and Winberry, 2017). It is important to understand the practical limitations of survey design in order to make decisions about future field experiments or to improve the processing of existing data sets.

To illustrate the consequences of different survey designs, we modified the ideal acquisition described in Fig. 5 in two independent ways: (1) shortening the array length, L, from 390 m to 190 m to represent a logistically constrained field location (e.g., crevasse fields limit array aperture); and (2) reducing the number of receivers from 400 to 40 stations and thereby increasing the spatial sampling interval, Δr_x, from 1 m to 10 m to represent a weight-limited field expedition (e.g., helicopter supported). Fig. 10 illustrates the modified acquisitions, and Fig. 11 presents the associated DPs generated from conditioned data after applying the direct-wave removal and offset-windowing steps that provide more reliable results.

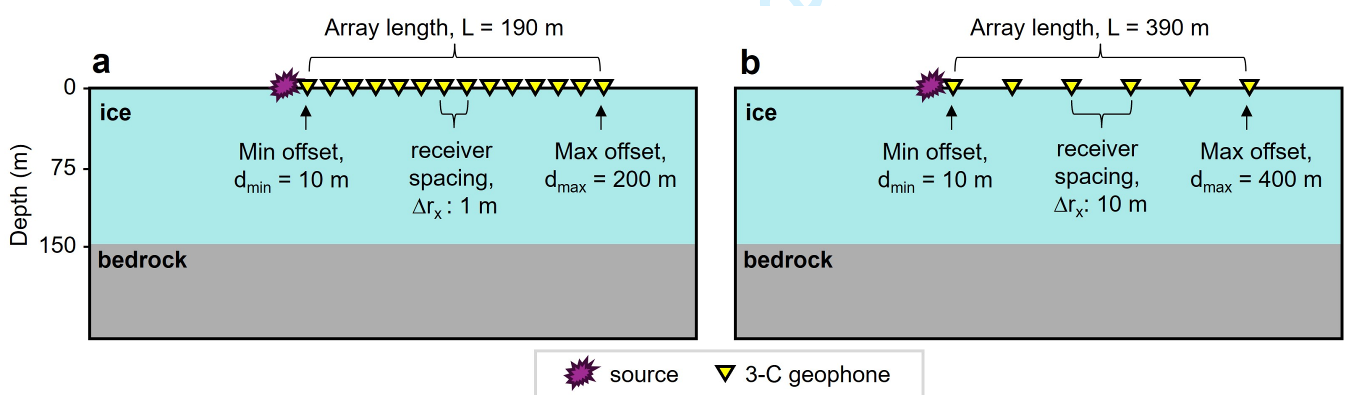

Fig. 10. Two-layer ice-bedrock model described in Table 2 with two different acquisition experiments: (a) an aperture of $L = 190$ m (approximately half the length of the example described in Fig. 5) and a receiver spacing of $\Delta r_x = 1$ m with the zero-offset receiver removed; and (b) an aperture of $L = 390$ m and a receiver spacing of $\Delta r_x = 10$ m. Not drawn to scale with the receiver placement only approximate for visual reference.

The shorter array reduces DP resolution across all frequencies, with a more pronounced effect at lower frequencies (Fig. 11a, 11b). Additionally, the maximum depth of investigation is now restricted to between 63 m and 95 m according to Eqn. (9) and, although the experimental picks between 5 Hz and 10 Hz (for the R component in particular) may seem accurate, their alignment in this study is coincidental. In complex models where higher-order modes are needed to characterize low-velocity or thinner layers, the poor resolution caused by the short aperture can hinder the identification of separate modes, ultimately restricting the effectiveness of the MASW method.

Greater receiver spacing (Fig. 11c, 11d) has less critical impact on DP resolution than a smaller-aperture survey. Larger receiver spacing primarily limits higher-frequency data according to Eqn. (8). In this experiment, however, 10 m-spacing is not a limiting factor for resolving the 150 m thick ice layer.

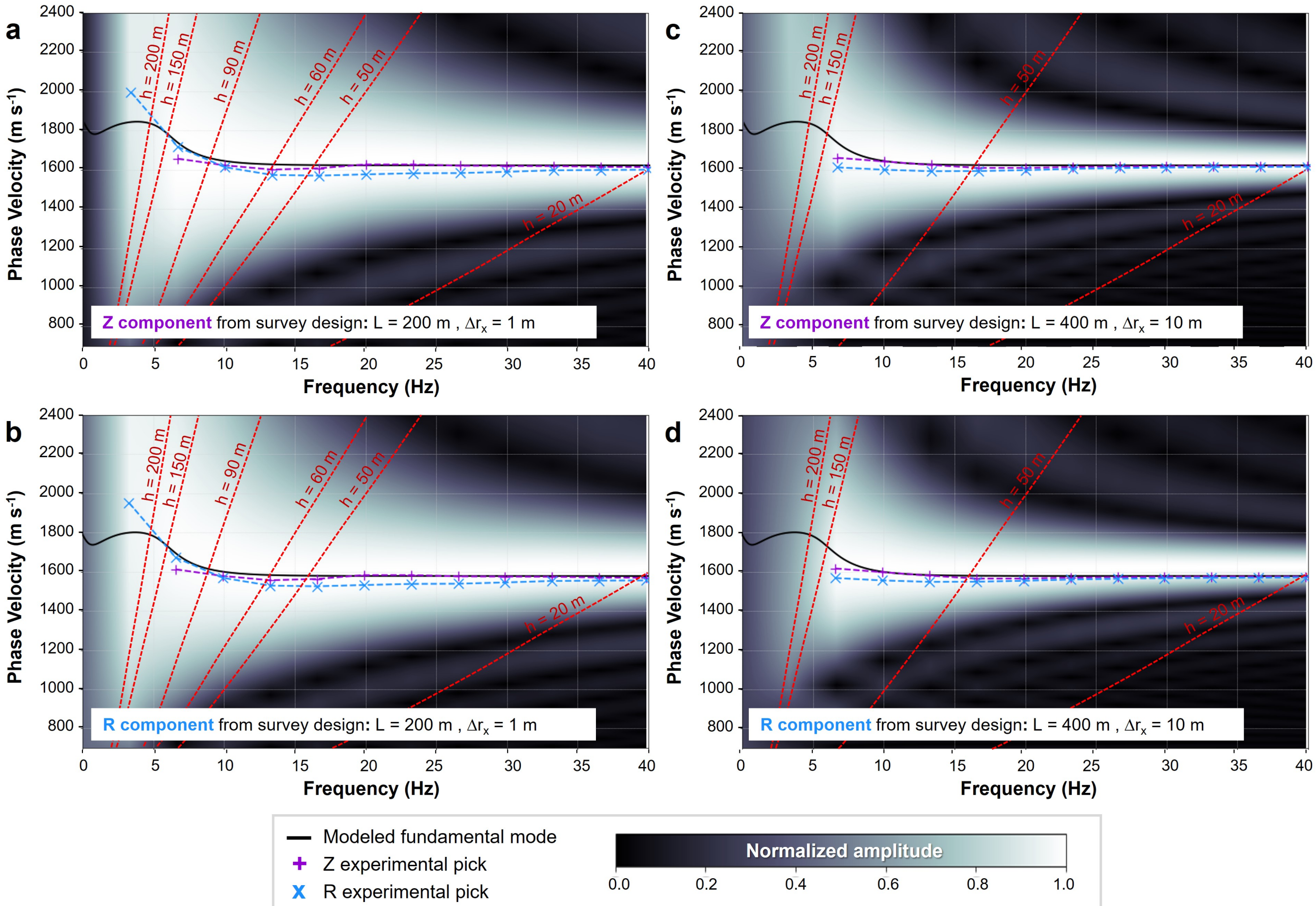

Fig. 11. Dispersion panels for Z- and R-component data from the two experiments described in Fig. 10. We conditioned data by removing the direct P-wave arrival and windowing to capture the full Rayleigh-wave signal at all offsets. (a) Z- and (b) R-component dispersion panels for shorter aperture ($L = 190$ m) experiment with dense ($\Delta r_x = 1$ m) receiver sampling; The resulting dispersion panels are lower resolution compared to the those generated from the ideal acquisition (Fig. 9). (c) Z- and (d) R-component dispersion panels for longer aperture experiment ($L = 390$ m) with sparse ($\Delta r_x = 10$ m) receiver sampling showing comparably lower data distortion than for the limited aperture case.

This first synthetic study has shown the impact that data conditioning steps and acquisition parameters have on estimating DCs, including the differential effect on Z- compared to R-component data. In these noise-free simulations, Z-component data are sufficient for MASW analysis; however, R-component data may offer more value than just boosting the data SNR. We explore this below using data from more complex synthetic and field experiments.

Study 3: DC Sensitivity to Shallow Complexity

We now seek to understand the value of well-conditioned MC data to characterizing more complex glacial environments such as a firn-aquifer system. Killingbeck and others (2020) motivates the importance of these aquifers for evaluating water-storage capacity and understanding meltwater dynamics at the Helheim Glacier, Greenland. Using 1-C geophone data and a multi-modal Bayesian inversion approach constrained by radar and borehole measurements, they mapped the spatial and depth variations in V_s from which the aquifer thickness was interpreted. We use their results to build a four-layer elastic model for evaluating the effectiveness of an MC-MASW approach to velocity modeling.

Our "base" model (Fig. 12a) consists of a 20 m firn layer overlying a 10 m-thick aquifer. For consistency with the previous investigation, we add bedrock at 150 m (much shallower than the true bed of Helheim Glacier). We also examine two model variations: (1) a "deep aquifer" model—an aquifer at 40 m with a thicker overlying firn layer (Fig. 12b); and (2) a "thick aquifer" model—an aquifer twice as thick as the "base" model but with the top remaining at 20 m (Fig. 12c).

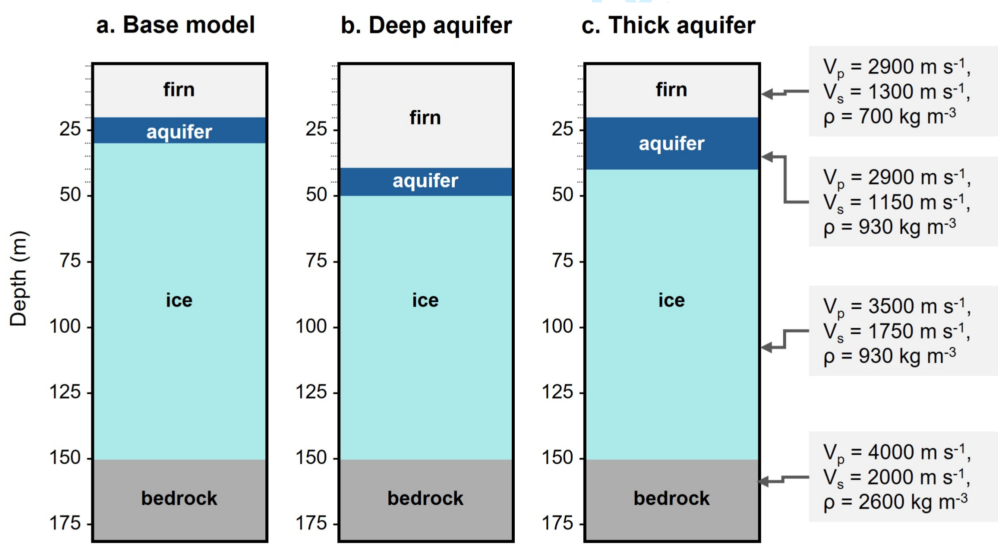

Fig. 12. Firn-aquifer model variations for synthetic data generation. (a) "Base" model derived from Helheim Glacier seismic inversion results (Killingbeck and others, 2018) with a 10 m thick aquifer overlain by 20 m of firn and a bedrock half-space imposed at 150 m depth. (b) "Deep Aquifer" model similar to (a) but with the firn layer extended to a depth of 40 m. (c)"Thick Aquifer" model similar to (a) but with the aquifer thickened to 20 m.

We simulated elastic shot-gather data using idealistic acquisition parameters: $\Delta r_x = 1$ m spacing and $L = 300$ m aperture. We condition the synthetic data by removing the near-offset traces (from 0 to10 m and effectively reducing L to 290 m) and direct arrivals and windowing appropriately to capture untruncated Rayleigh wave arrivals on each trace (Fig. 13).

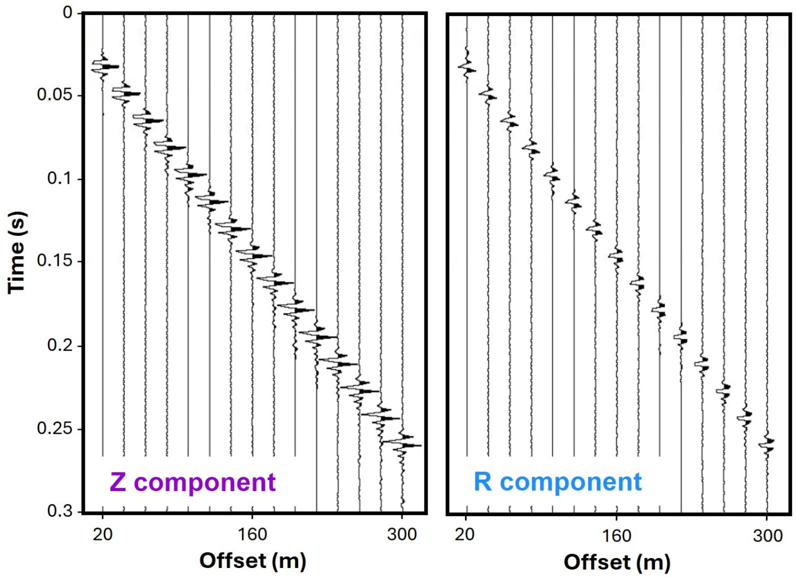

Fig. 13. Conditioned Z- and R-component shot gathers for the "base" firn-aquifer model described in Fig. 12. Every 20th trace is plotted for offsets ranging from 20 m to 300 m.

Fig. 14 first compares the Z- and R-components numerical solutions for the fundamental mode of the three firn-aquifer models (Fig. 14a), with separate comparisons of the experimental picks to the numerical solutions of the fundamental mode for each model (Fig. 14b-14d). The numerical solutions for the three models are quite similar and in particular, discerning between the deep (blue) and thick (pink) models would require high-resolution DPs and accurate experimental picks within the $8 - 20$ Hz range. Within this range, however, both the Z- and R-component experimental DCs (+ and x, respectively, on Fig. 14b–14d) significantly deviate from the numerical solution.

For all models, the Z-component experimental DCs have a stronger gradient than R-component DCs. To understand why these picks differ and how this relationship may change for each dataset, we examine the depth-sensitivity kernels at different frequencies (Fig. 15). We note that the U_z sensitivities (Fig. 15a–15f) are generally similar for all three models: for frequencies above 10 Hz, U_z is most sensitive (highest eigenfunction amplitude) to the shallow firn layer and under 10 Hz, U_z is sensitive to deeper structure. The largest difference between U_z kernels for the models are between 10 Hz and 17 Hz. For all models, the strongest negative U_x sensitivities are at the surface and generally, the depths at which U_x sensitivity is maximum and positive are deeper than the corresponding U_z sensitivity. Additionally, the U_x kernels (Fig. 15g–15l) exhibit two characteristic signatures for all three models not observed on the U_z kernels: (1) 9.95 Hz and 13.27 Hz sensitivities show h_r changes per model at different frequencies; and (2) for all frequencies, there are inflection points in sensitivity that occur at depths (consistently at all frequencies) that correlate to the base of the aquifer (dotted lines).

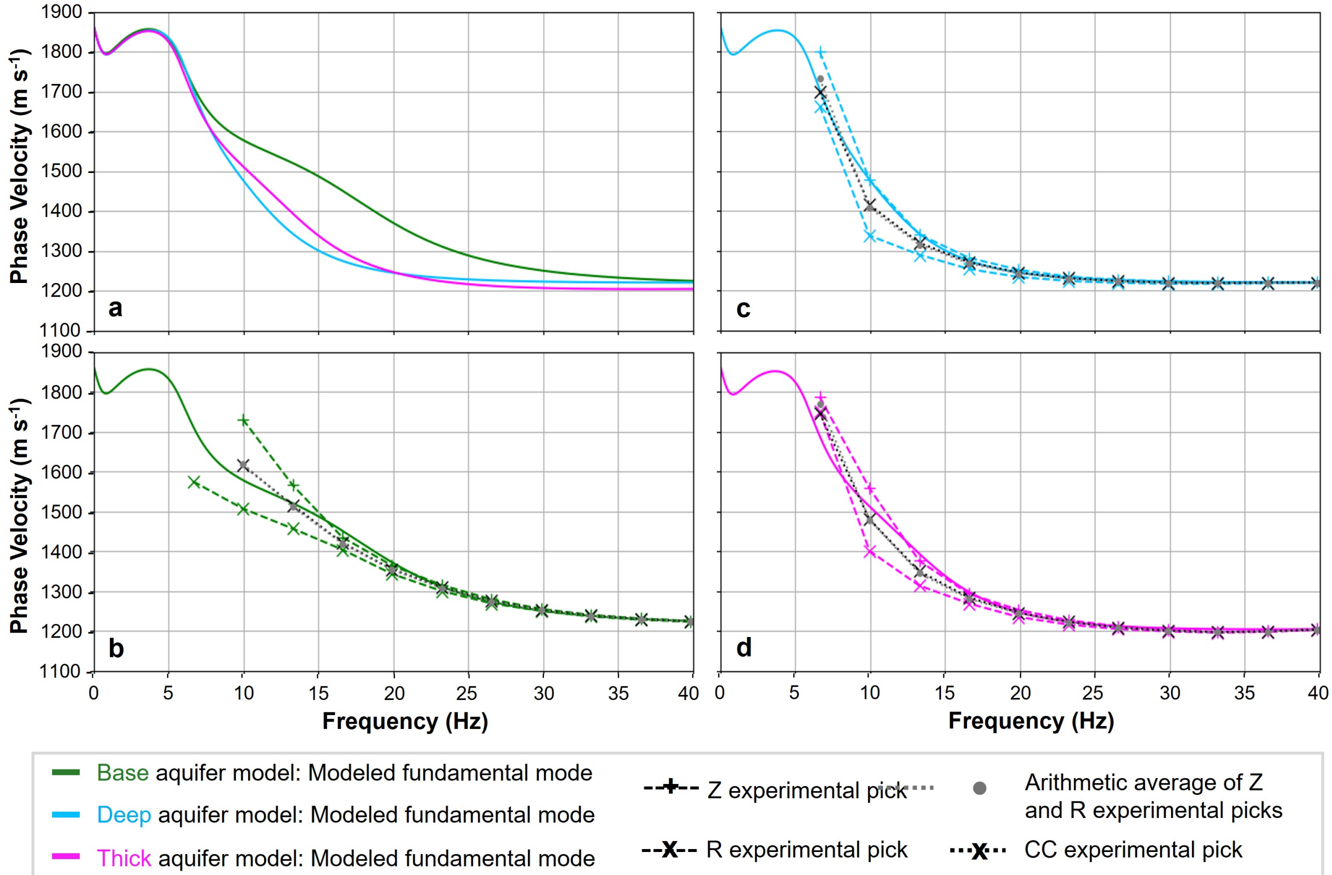

Fig. 14. Numerical solutions and experimental DCs of the fundamental mode associated with the three models described in Fig. 12. (a) Numerical solution of the fundamental DC for base (green), deep aquifer (cyan), and thick aquifer (magenta) models. Z- and R-component DCs for the (b) base, (c) deep aquifer, and (d) thick aquifer models, with experimental picks for Z- (plus symbols) and R-component (cross symbols), the arithmetic average of Z- and R-component phase velocity (grey circles), and the complex conjugate (CC) of Z- and R- components (black cross symbols). Between 8 and 20 Hz, the variability of DCs for the three models suggests that accurate picks in this frequency band are important for mitigating the non-uniqueness of dispersion analysis and inversion.

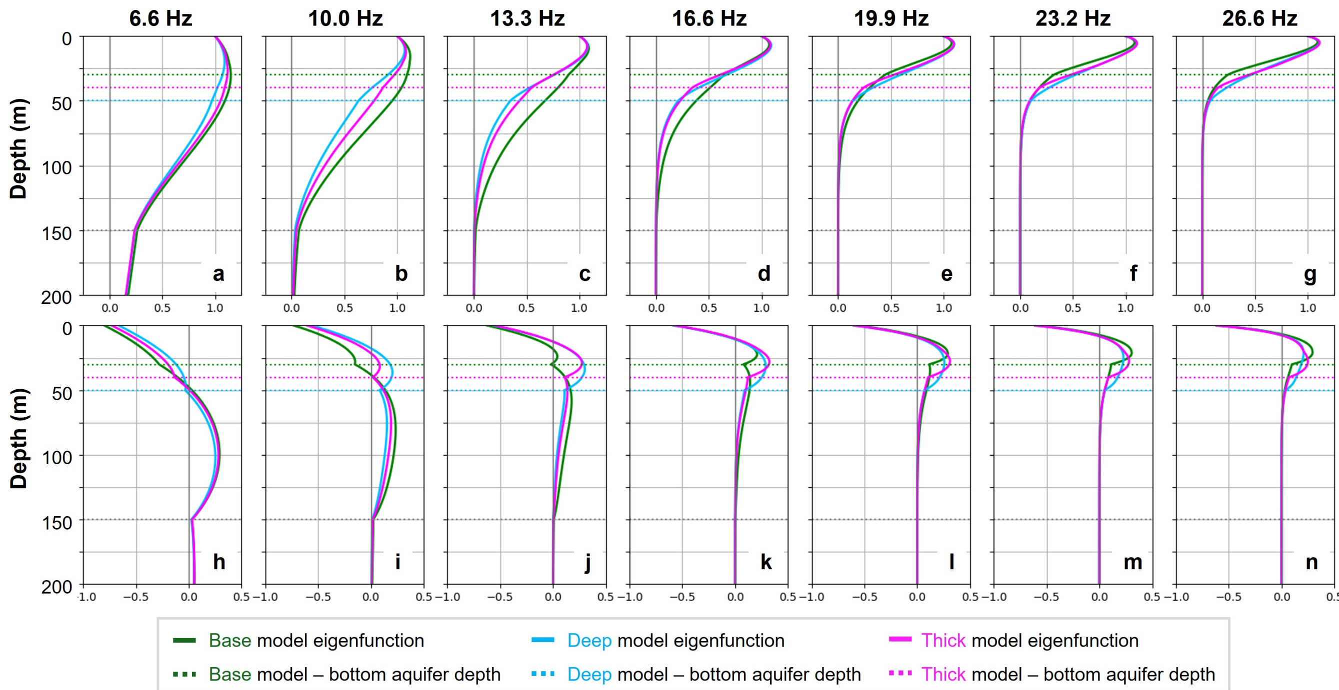

Fig. 15. Depth sensitivity kernels for discrete frequencies of the three aquifer-firn experiments described in Fig. 12. (a–g) U_z components. (h–n) U_x components. Depths of the bottom of aquifer are color coded for each model, and the depth of the ice-bedrock interface is shown with a dotted gray line at 150 m. The unique sensitivities of the U_x curves for each model motivate an opportunity for improving MASW inversion accuracy through use of MC data.

Combining MC data

To exploit the unique depth sensitivities of both U_z and U_x, we use the complex conjugate (CC) summation to combine the orthogonal components in the shot-gather domain. We calculate a CC component as

$$CC(d, t) = Z(d, t) + iR(d, t) \ . \tag{10}$$

Experimental picks for the CC component are plotted on Fig. 14 for each respective firn model (black dotted lines with black crosses). Compared to the individual Z- and R-component picks, the CC picks very closely track the numerical solutions for all models. We also calculate an arithmetic mean of the Z and R experimental picks (gray dotted lines with gray dots) where there is no implicit account for orthogonality and each component is equally weighted. For these idealistic experiments the CC picks and arithmetic averages are almost identical with the exception of the 6 Hz pick (near the low frequency acquisition limit) on the "deep-" and "thick-aquifer" experiments where the CC picks are slightly more accurate.

We observed that the Z- and R-component DCs differ due to their variable depth sensitivities. For all the firn-aquifer models examined, the R-component DC picks tend to be lower than those from the

Z component and an arithmetic average offered a more representative solution. Although not a concern in these ideal synthetic experiments, where DPs are poor resolution, this averaging may additionally help mitigate SNR-related picking errors. Moreover, our proposed CC summation method, which honors the orthogonal nature of the components, may outperform the arithmetic averaging as it potentially better exploits the unique depth sensitivities inherent to each displacement component. We evaluate this hypothesis and apply other insights derived from the synthetic studies to a MC field dataset acquired on the Saskatchewan Glacier in the Canadian Rocky Mountains.

RESULTS: FIELD EXPERIMENT ON SASKATCHEWAN GLACIER

This section assesses the effectiveness of the MC dispersion analysis under real-world conditions, focusing on how well the data conditioning workflow and techniques for integrating Z- and R-component data handle the complexities of field seismic surveys (constrained by array length, limited receivers, and imperfect data quality).

Survey details

In August 2019, Stevens and others (2023) acquired a 2-D active-seismic survey on the Saskatchewan Glacier (Fig. 16) to supplement other geophysical investigations focused on basal ice dynamics. The acquisition used nine 3-C geophones (R1 to R9) spaced $\Delta r_x = 10$ m apart forming a linear array of $L = 80$ m aperture oriented along the glacier's centerline. A sledgehammer impacting a metal plate served as a seismic energy source at 25 station locations (S01 to S25) distributed over a 240 m span centered on the array with a maximum two-sided offset of $d_{max} = 160$ m. A tenth 3-C geophone was moved to every source station to record the excitation time of each shot.

Data conditioning

Fig. 17 presents examples of raw Z- and R-component shot gathers for station S02. We note the presence of a noisy zero-offset trace and the absence of traces at receivers R2 and R9. These data issues reflect the inherent challenges in field experiments arising due to equipment malfunction. Without managing data errors appropriately, the Z- and R-component DPs are inaccurately complex and noisy (Fig. 18a, 18b).

Building on synthetic study insights, we mute the direct wave and insert zero traces at the missing trace locations. This results in a substantial improvement in the quality of the S02 Z- and R-component DPs

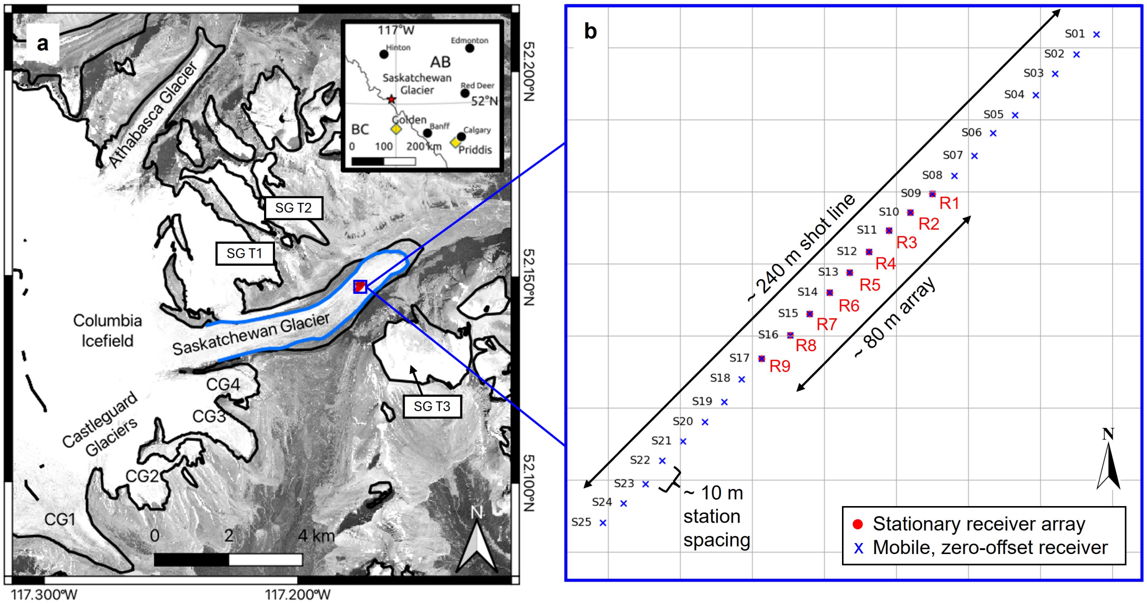

Fig. 16. (a) Saskatchewan Glacier location in the Canadian Rocky Mountains, Canada (see inset map). Basemap imagery: Orthorectified 4-band PlanetScope scene accessed via Planet.com (b) Geometry of the active-source seismic experiment conducted in the ablation zone involving a stationary array of nine 3-C geophones (R1-R9) linearly spaced at 10 m to form an array of aperture $L = 80$ m. Source station locations S01-S25, also spaced 10 m apart, are shown as blue Xs.

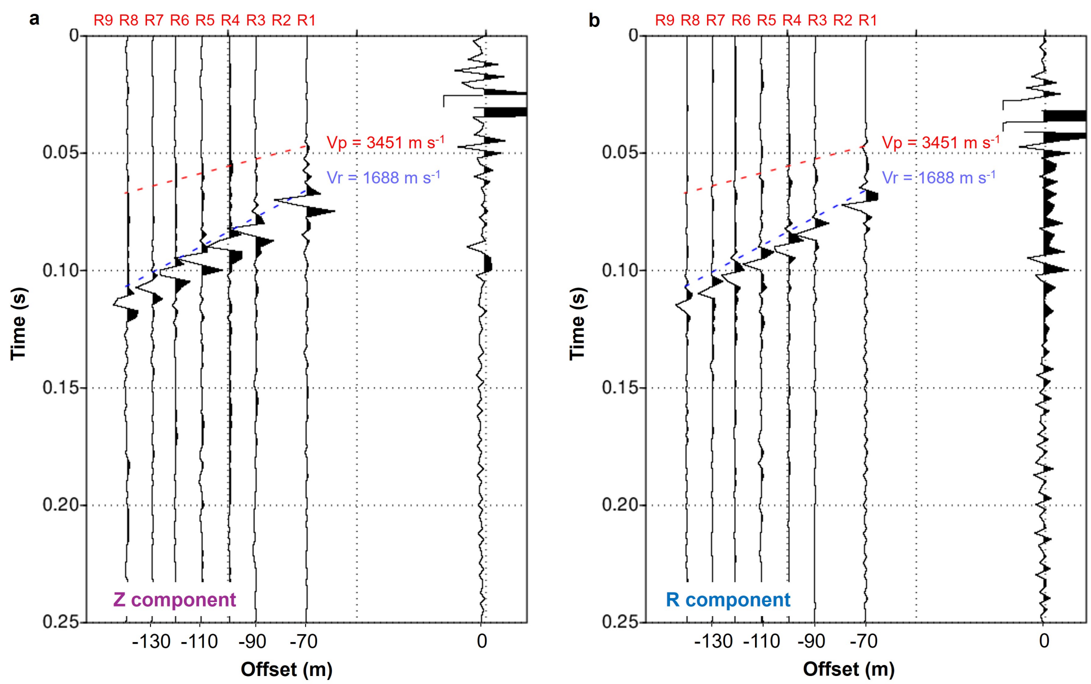

Fig. 17. (a) Raw Z- and (b) R-component shot-gather data for station S02. The zero-offset trace recorded by the mobile geophone is used to window the continuously recorded data on geophones R1-R9 into shot gathers. V_p and V_r moveout velocities calculated by Stevens and others (2023) are plotted. Note the missing traces at R2 and R9. Additionally, direct P-wave arrival is weaker on the Z- versus the R-component because of the predominantly horizontal particle motion. Strong Rayleigh wave energy is recorded on both components.

(Fig. 18c, 18d). Fig. 18e and 18f show Z- and R-component DPs for station S05, and Fig. 18g and 18h show Z- and $R-$ component DPs for station S09. The infilled zero traces however impose a beat-like signature on the DPs. A more optimal conditioning approach would be to infill this trace through interpolation or supergather processing (Hesthammer and Løkkebø, 1997).

Supergather processing

Supergather processing provides a means to infill missing offset traces (Hesthammer and Løkkebø, 1997) but additionally, it extends effective array aperture thereby improving the resolution of the DPs for dispersion analysis. To build a supergather from several shots, each gather is first windowed to align traces of the same offsets by applying time-shifts as necessary to each shot gather. The time-shifted gathers stacked by averaging traces at similar offsets. Fig. 19 illustrates the supergather approach where the Z-component gathers at stations S02, S05, and S09 are time-aligned (Fig. 19a) and then stacked (Fig. 19b). The resulting effective supergather aperture is $L = 130$ m (i.e., 50 m longer than the stationary receiver array) with no missing trace information. Fig. 18i and 18j show the Z- and R-component DPs, respectively, constructed from the S02, S05, and S09 supergathers. The resolution of the resulting DPs is substantially improved compared to the single-gather DPs (Fig. 18c–18h) leading to higher confidence experimental picks.

We generate the DP from the CC summation of the Z- and R-component supergathers (Fig. 20a) and compare the experimental DC picks of the Z, R, and CCcomponents with the arithmetic average of the Z- and R-component data (Fig. 20b). The largest differences are observed sub-50 Hz. Generally, the combination methods (CC and average) result in smoother DCs versus the single-component picks.

The average and CC picks are similar between $40 - 150$ Hz and the differences observed outside this range could result from higher DC uncertainty due to poorer DP resolution. Following observations from the four-layer synthetic study, near the limiting acquisition frequencies we might expect the CC picks to be more reliable. This is possibly a rationale for the smoother CC DC trend between $25 - 40$ Hz versus that of the average.

An alternate method for reducing experimental pick uncertainties is presented by Olafsdottir and others (2018a) and included in the *MASWaves* software. This approach calculates a mean DC from individual DP picks by averaging over user-defined, logarithmically spaced wavelength bins.

Using the conditioned S02, S05, and S09 panels presented in Fig. 18, we perform this weighted-mean DC approach and compare the experimental picks to those of the arithmetic-mean- and CC-supergather DPs

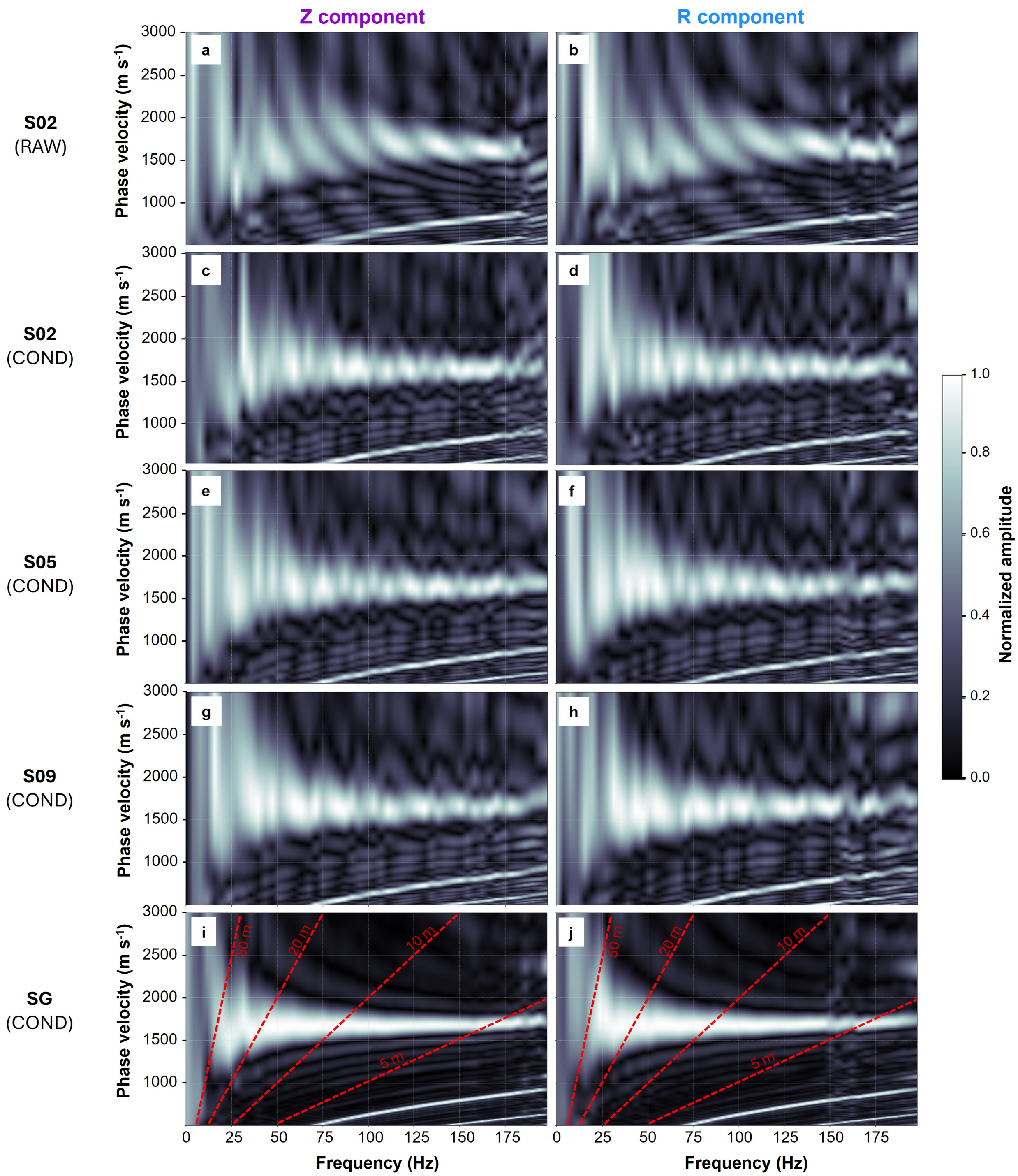

Fig. 18. Raw (a) Z- and (b) R-component DPs for the S02 shot gathers shown in Fig. 17. Conditioned (c) Z- and (d) R-component DPs corresponding to (a) and (b) after removing the zero-offset traces, muting the direct wave, and infilling missing traces with a zeroed trace. Conditioned (e) Z- and (f) R-component DPs at station S05 and (g) Z- and (h) R-component for station S09. Conditioned (i) Z- and (j) R-component supergather DPs combining S02, S05, and S09 shot-gather data. The conditioned individual shots produce consistent DCs although a beat-like signature is imposed as a result of the zeroed infill trace and no interpolation. The supergather DC infills missing offsets and extends the effective array aperture producing higher-resolution DPs.

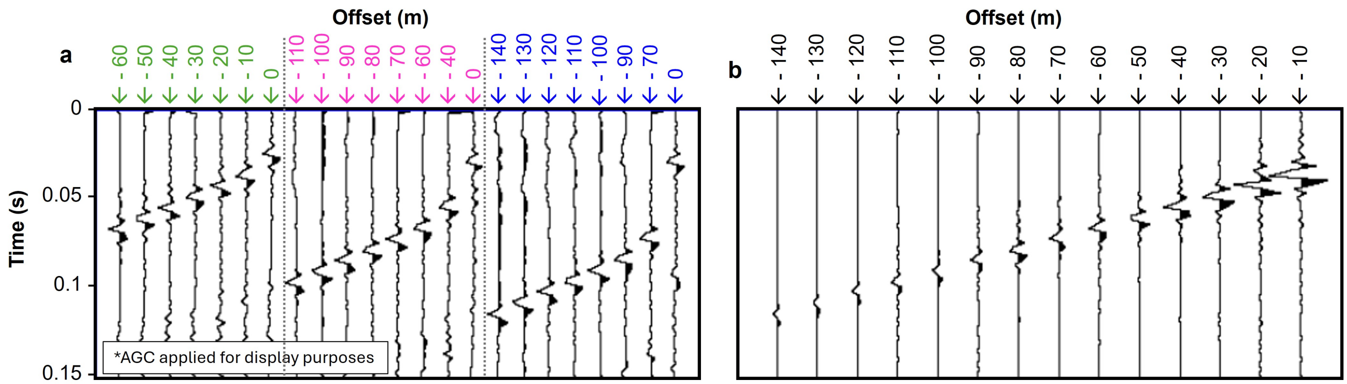

Fig. 19. (a) Time-aligned Z-component shot gathers for stations S02 (blue), S05 (pink), and S09 (green) with differing offset ranges (x-axis labels). (b) Supergather produced from stacking the three shots in (a) based on similar offsets thus increasing the effective array aperture to L = 130 m and infilling missing offset traces without interpolation.

(Fig. 20b). The bandwidths over which experimental picks can be reliably identified are similar between all three approaches. The *MASWaves* weighted-mean DC picks under 50 Hz fluctuate substantially, suggesting low confidence in the results. Above 50 Hz, these experimental DCs are flat with lower V_r values than those of the arithmetic average or CC component. We note that the weighted-mean DC picks in this range are highly sensitive to the selected bin window.

Qualitative Interpretation of DC

We first consider the resolution limitations of the survey, noting that the empirical estimates presented in the Theory section have been validated for typical ice velocities. For an array length of L = 130 m, the maximum resolvable depth is approximately 43–65 m (Eqn. 9), which is insufficient for detecting a bedrock interface expected at depths greater than 100 m (Stevens and others, 2023). This depth range aligns with the 20 Hz low-frequency limit of the DCs presented in Fig. 18b. Similarly, the minimum resolvable depth, estimated at 5 m for a receiver spacing of 10 m (Eqn. 8), is consistent with the inability to make reliable picks above $\sim$ 165 Hz. This is evidenced by the observable increase in noise on the DP (Fig. 18a) and the apparent increase in V_r with frequency on the DC which are both likely due to aliasing.

High-confidence picks between 40 Hz and 165 Hz on the CC supergather yield a mean V_r value of 1670 ± 10 m s^{-1}, suggesting that the ice column is potentially vertically homogeneous between 5 m to 20 m. This estimate is fairly similar to the linear moveout velocity of 1690 m s^{-1} reported by Stevens and others (2023). Notably, this interpretation of apparent homogeneity is drawn from a single supergather using only a small subset of shots from a 60 m active-source seismic spread. In cases where subsurface conditions

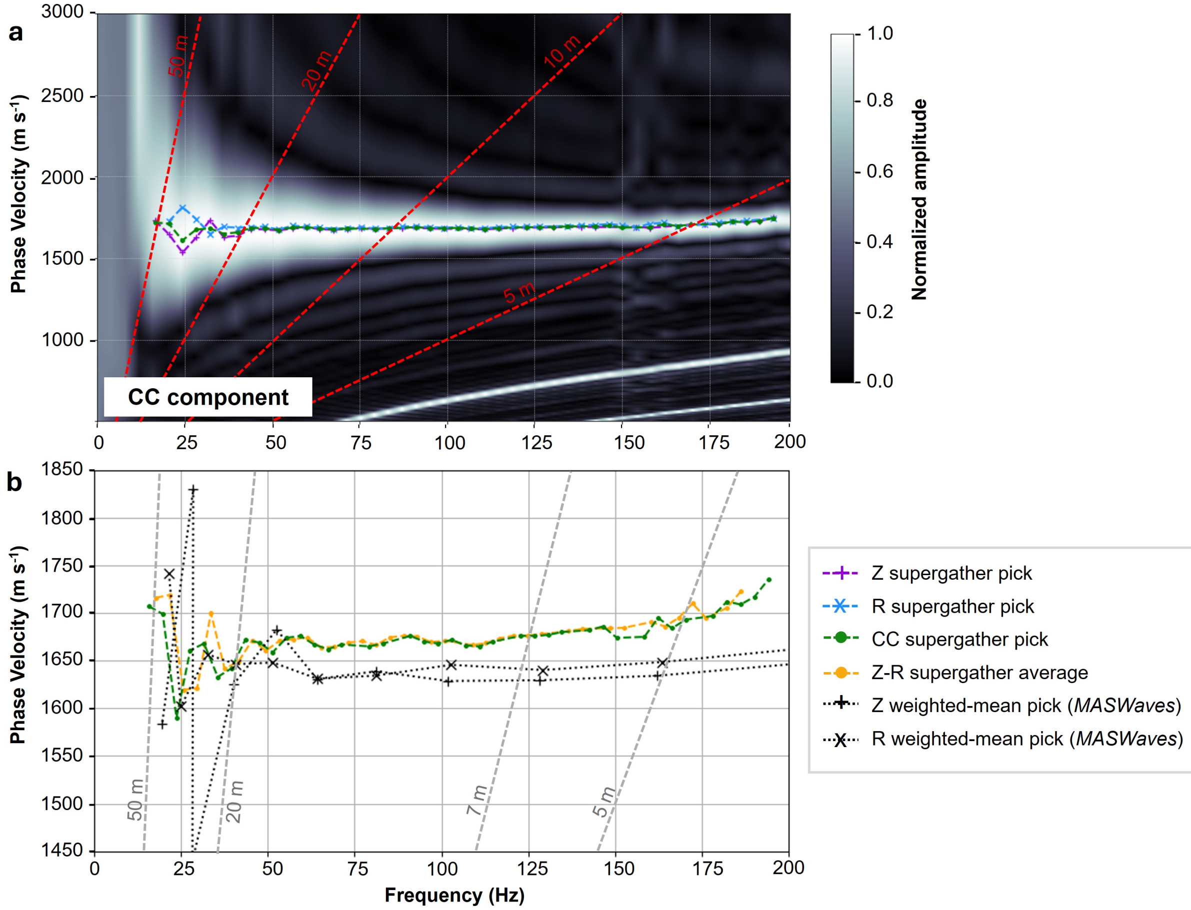

Fig. 20. (a) Dispersion panel derived from CC supergather from shots 02, 05 and 09. (b) Comparison of experimental dispersion curve picks from CC supergather (dashed black line) and individual Z- and R-components (+ and x symbols, respectively), the arithmetic mean (black dots), and the weighted-mean picks calculated from the internal *MASWaves* algorithm (dark and light purple for Z and R components, respectively). All picks were made on the respective DC panels (Fig. 18) using the standard picking algorithm in the *MASWaves* software. There is little evidence of dispersion and the experimental picks suggest an average $V_r = 1670$ m s^{-1} between 40 and 165 Hz.

are unknown, qualitative DP analyses can quickly indicate whether a uniform ice velocity assumption is reasonable (based on consistency with empirical velocity estimates or linear moveout) and whether inversion is necessary to resolve vertical layering inferred from observed V_r–f gradients in the panel.

Inversion is not only essential for mapping phase-velocity trends into V_s–depth profiles, but it may also help constrain reasonable solutions in frequency ranges where dispersion picks are uncertain and qualitative analysis is limited. In our case, the 20 Hz to 40 Hz band is sensitive to depths of approximately 20 m to 50 m exhibits more variable picks, with a mean phase velocity of 1650 ± 30 m s^{-1}. This could indicate a slight decrease in velocity with depth, although the trend may also reflect noise or errors in the pick estimates. A formal inversion may help determine whether these variations are attributable to a plausible subsurface model or whether they are simply artifacts of lower signal-to-noise conditions at these frequencies.

DISCUSSION

The feasibility studies presented herein highlight the subtle differences in DCs arising from different preprocessing methods and subsurface layer complexity. These results underscore the inherent non-uniqueness of dispersion analysis and inversion, a challenge well-documented in prior studies. For example, de Lucena and Taioli (2014) conducted a detailed synthetic investigation into dispersion curve sensitivities, emphasizing the importance of inversion parametrization and initial model choice. With a focus on active-seismic glacial experiments, our study emphasizes improving the forward problem by optimizing acquisition strategies, refining data conditioning, and harnessing the advantages of MC datasets.

Acquisition design recommendations

We demonstrate that prioritizing array aperture over receiver spacing is judicious for Rayleigh-wave dispersion analysis, enhancing both the depth of investigation and DP resolution. For instance, with a setup of ten geophones targeting a firn aquifer with a top depth of 40 m, setting the receiver spacing to half the shallowest depth of investigation (20 m in this case) will suffice and the receiver array can be as long as 180 m. To further optimize offset coverage, a denser shot spacing can be employed. For example, at 20 m receiver spacing, initiating shots every 10 m enables data acquisition at offsets of 10 m intervals.

Supergathers and data conditioning

Supergathers aggregate Rayleigh-wave data from multiple shot locations to enhance signal quality, infill missing traces, and extend effective array aperture and thereby the depth of investigation. Although alternative methods such as the weighted-mean calculation presented by Olafsdottir and others (2018a) offer results with frequency bandwidth similar to the supergather approach, the dispersion curves picks exhibit higher uncertainty, greater variance, and an increased dependence on the particular window selected for data binning and averaging. Beyond increasing SNR and improving picking confidence, supergathers inherently infill missing offsets and reduce (or fully obviate) the need for data interpolation.

A common drawback across all methods is that, in areas with lateral heterogeneity or structural complexity, spatial averaging of data points can obscure subtle subsurface features and reduce the accuracy of derived models. As such, the choice of processing strategy should be guided by the specific scientific objectives and the expected scale of variability. In surface wave analysis, DPs inherently average over the array aperture, making the trace mixing introduced by supergathers generally acceptable. However, a specific caveat with the supergather approach is that any misalignment of zero-offset traces can mask fine dispersive characteristics, underscoring the importance of applying appropriate timing corrections.

Horizontal-component contributions

The Z- and R-component data acquire orthogonal particle motions of Rayleigh waves. By leveraging both, the complete elliptical particle motion of Rayleigh waves can be reconstructed. At a fundamental level, we have identified two key mechanisms through which the R-component Rayleigh-wave energy enhances dispersion analysis. First, the R component provides an additional dataset for capturing dispersion at the same locations as the Z component, thereby increasing the accuracy of experimental picks by increasing the overall data volume. Although phase shifts between the Z- and R-component data complicate direct stacking, averaging the individual experimental picks from both components can yield more reliable results. This approach mitigates the impact of erroneous picks that may arise from poor SNR, improving the robustness of dispersion analysis. Second, R-component data exhibit complementary sensitivity to subsurface layering, offering insights into layered media indiscernible from Z-component data alone. We have observed that the depth at which the sense of elliptical particle motion reverses varies with different layer complexity and, at low frequencies, there are potentially multiple depths at which the sense of motion reverses direction. In addition, where strong V_s variations exist (e.g., at the ice-bedrock or firn-aquifer-ice interfaces), we observe inflection points on the U_x-depth sensitivity kernel that indicate localized narrowing or widening of the particle motion ellipticity. Moreover, these are sharpest at the frequencies exhibiting the strongest Rayleigh-wave dispersion effects (Lay and Wallace, 1995) and are thus functions of the depth and $V_s(z)$ contrast of subsurface velocity layering.

These sensitivities of the horizontal Rayleigh-wave displacement underscore the critical role of the R component in advancing the accuracy of MASW inversion using active-source seismic investigations. Finger and Löer (2024) noted the correlation between the extrema of ellipticity to sudden velocity changes and demonstrated its utility in $V_s(z)$ profiling using ambient seismic data. This motivates the integration of ellipticity information in active-seismic methods such as MASW to increase the resolution of near-surface velocity structure.

CONCLUSIONS

Our feasibility studies provide actionable insights for glaciologists, offering guidance on survey design and data conditioning to enhance data quality. We highlight the advantage of longer receiver arrays on the quality of dispersion curves and validate rule-of-thumb approximations for the minimum and maximum depths of investigation as well as the depth of elliptical rotation reversal in glacial regimes in comparison to those of shallow soil models and Poisson solids. Furthermore, we outline critical data conditioning steps for enhancing Rayleigh-wave dispersion analysis. Key procedures include removing the zero-offset trace and windowing shot gathers to avoid truncating the Rayleigh-wave arrivals on all traces. When using multi-component data, rotating data to radial-transverse coordinates and muting the direct wave also are important steps. Interpolating or infilling missing traces (often unavoidable in field experiments) is critical for generating accurate dispersion curves. Using field data from the Saskatchewan Glacier, we demonstrate how building supergathers (under reasonable assumptions of lateral homogeneity) can be effective for infilling missing traces while improving dispersion-panel (and therefore dispersion-curve) resolution by increasing the effective array aperture.

Using multi-layered firn-aquifer models, we demonstrate how MC geophone records can improve the detection of englacial structures. Averaging experimental picks from the radial and vertical components can mitigate errors associated with low signal-to-noise ratios. Our depth-sensitivity analysis, though, reveals that the horizontal displacement of elliptical particle motion contains complementary information not captured by the vertical component data alone. Integrating horizontal displacement data in an MC-MASW analysis potentially could help differentiate aquifer thickness and depth, beyond the ability of single vertical-component geophone analysis.

DATA AVAILABILITY

Synthetic glacial datasets and models are available on GitHub (https://github.com/samara-melody/MC-MASW), alongside relevant processing scripts. We refer the reader to Stevens and others (2023) and their accompanied supplemental material for information regarding accessibility of the Saskatchewan Glacier field datasets.

ACKNOWLEDGMENTS

The Mines Geophysics Department, Mines Glaciology Laboratory and Center for Wave Phenomena each supported the author's research through scholarship. The author gives special thanks to H. Verboncoeur and N. Punithan for insightful discussions and shared domain knowledge.

Analyses in this work were conducted using a range of open-source software packages. We acknowledge the efforts of the developers and contributors who advance accessible tools for scientific research. We used the software *MASWaves* (Olafsdottir and others, 2018b) for dispersion curve forward modeling and analysis and *disba* for numerical modeling. We carried out seismic data processing using *ObsPy* (Beyreuther and others, 2010) for field data in MiniSEED format and *Seismic Unix* for SEGY-formatted data (Stockwell Jr, 1999). Additional numerical and symbolic computations, as well as data visualization, were supported by Python libraries including *NumPy* (Harris and others, 2020), *SymPy* (Meurer and others, 2017), *pandas* (McKinney, 2010) and *Matplotlib* (Hunter, 2007).

REFERENCES

Agnew RS, Clark RA, Booth AD, Brisbourne AM and Smith AM (2023) Measuring seismic attenuation in polar firn: method and application to Korff Ice Rise, West Antarctica. *Journal of Glaciology*, **69**(278), 2075–2086 (doi: 10.1017/jog.2023.82).

Aki K and Richards PG (2002) *Quantitative Seismology*. University Science Books, ISBN 0935702962.

Ammon CJ, Velasco AA, Lay T and Wallace TC (2020) *Foundations of Modern Global Seismology*. Academic Press, ISBN 0128156791.

Aster RC and Winberry JP (2017) Glacial seismology. *Reports on Progress in Physics*, **80**(12), 126801 (doi: 10.1088/1361-6633/aa8473).

Bennett MR (2022) *Our Dynamic Earth: A Primer*. Springer International Publishing, Cham, ISBN 3030903532 (doi: 10.1007/978-3-030-90351-0_9).

Beyreuther M, Barsch R, Krischer L, Megies T, Behr Y and Wassermann J (2010) ObsPy: A Python toolbox for seismology. *Seismological Research Letters*, **81**(3), 530–533.

Bohlen T, De Nil D, Köhn D and Jetschny S (2016) SOFI2D seismic modeling with finite differences: 2D—elastic and viscoelastic version. *user guide*, accessed: 2024-03-01.

Church G, Bauder A, Grab M, Rabenstein L, Singh S and Maurer H (2019) Detecting and characterising an englacial conduit network within a temperate Swiss glacier using active seismic, ground penetrating radar and borehole analysis. *Annals of Glaciology*, **60**(79), 193–205 (doi: 10.1017/aog.2019.19).

Crice D (2005) MASW, the wave of the future editorial. *Journal of Environmental & Engineering Geophysics*, **10**(2), 77–79 (doi: 10.2113/JEEG10.2.77).

de Lucena RF and Taioli F (2014) Rayleigh wave modeling: A study of dispersion curve sensitivity and methodology for calculating an initial model to be included in an inversion algorithm. *Journal of Applied Geophysics*, **108**, 140–151 (doi: 10.1016/j.jappgeo.2014.07.007).

Finger C and Löer K (2024) Depth of sudden velocity changes derived from multi-mode Rayleigh waves. *Journal of Geophysical Research: Solid Earth*, **129**(3), e2023JB028322 (doi: 10.1029/2023JB028322).

Foti S, Hollender F, Garofalo F, Albarello D, Asten M, Bard PY, Comina C, Cornou C, Cox B, Di Giulio G and others (2018) Guidelines for the good practice of surface wave analysis: a product of the InterPACIFIC project. *Bulletin of Earthquake Engineering*, **16**, 2367–2420 (doi: 10.1007/s10518-017-0206-7).

Harris CR, Millman KJ, der Walt SJ, Gommers R, Virtanen P, Cournapeau D, Wieser E, Taylor J, Berg S, Smith NJ, Kern R, Picus M, Hoyer S, van Kerkwijk MH, Brett M, Haldane A, del Río JF, Wiebe M, Peterson P, Gérard-Marchant P, Sheppard K, Reddy T, Weckesser W, Abbasi H, Gohlke C and Oliphant TE (2020) Array programming with NumPy. *Nature*, **585**(7825), 357–362 (doi: 10.1038/s41586-020-2649-2).

Hesthammer J and Løkkebø SM (1997) Combining seismic surveys to improve data quality. *First Break*, **15**(4).

Hunter JD (2007) Matplotlib: A 2D graphics environment. *Computing in Science & Engineering*, **9**(3), 90–95 (doi: 10.1109/MCSE.2007.55).

Ibs-von Seht M and Wohlenberg J (1999) Microtremor measurements used to map thickness of soft sediments. *Bulletin of the Seismological Society of America*, **89**(1), 250–259 (doi: 10.1785/BSSA0890010250).

Johansen TA, Ruud B, Bakke NE, Riste P, Johannessen EP and Henningsen T (2011) Seismic profiling on Arctic glaciers. *First Break*, **29**(2) (doi: 10.3997/1365-2397.20112st1).

Killingbeck S, Livermore P, Booth A and West L (2018) Multimodal layered transdimensional inversion of seismic dispersion curves with depth constraints. *Geochemistry, Geophysics, Geosystems*, **19**(12), 4957–4971 (doi: 10.1029/2018GC008000).

Killingbeck S, Schmerr N, Montgomery L, Booth A, Livermore P, Guandique J, Miller OL, Burdick S, Forster R, Koenig L and others (2020) Integrated borehole, radar, and seismic velocity analysis reveals dynamic spatial variations within a firn aquifer in southeast Greenland. *Geophysical Research Letters*, **47**(18), e2020GL089335 (doi: 10.1029/2020GL089335).

Koller M, Chatelain J, Guillier B, Duval A, Atakan K, Lacave C, Bard P and participants S (2004) Practical user guideline and software for the implementation of the H/V ratio technique on ambient vibrations: measuring conditions, processing method and results interpretation. In *13th World Conference on Earthquake Engineering*.

Kuehn T, Holt JW, Johnson R and Meng T (2024) Active seismic refraction, reflection, and surface-wave surveys in thick debris-covered glacial environments. *Journal of Geophysical Research: Earth Surface*, **129**(1), e2023JF007304 (doi: 10.1029/2023JF007304).

Lay T and Wallace TC (1995) *Modern Global Seismology*. Elsevier, ISBN 012732870X.

Liner C (2012) *Elements of seismic dispersion: A somewhat practical guide to frequency-dependent phenomena*. Society of Exploration Geophysicists, ISBN 156080291X.

Luu K (2021) DISBA: Numba-accelerated computation of surface wave dispersion (doi: 10.5281/zenodo.3987395), accessed: 2024-04-01.

McKinney W (2010) Data structures for statistical computing in Python. In *Proceedings of the 9th Python in Science Conference*, 51–56.

Meurer A, Smith CP, Paprocki M, Čertík O, Kirpichev SB, Rocklin M, Kumar A, Ivanov S, Moore JK, Singh S, Rathnayake T, Vig S, Granger BE, Muller RP, Bonazzi F, Gupta H, Vats S, Johansson F, Pedregosa F, Curry MJ, Terrel AR, Roučka v, Saboo A, Fernando I, Kulal S, Cimrman R and Scopatz A (2017) SymPy: symbolic computing in Python. *PeerJ Computer Science*, **3**, e103, ISSN 2376-5992 (doi: 10.7717/peerj-cs.103).

Olafsdottir EA, Bessason B and Erlingsson S (2018a) Combination of dispersion curves from MASW measurements. *Soil Dynamics and Earthquake Engineering*, **113**, 473–487 (doi: 10.1016/j.soildyn.2018.05.025), accessed: 2024-05-01.

Olafsdottir EA, Erlingsson S and Bessason B (2018b) Open software for analysis of MASW data. In *Proceedings of the 16th European Conference on Earthquake Engineering*, accessed: 2024-05-01.

Park CB, Miller RD and Xia J (1998) Imaging dispersion curves of surface waves on multi-channel record. In *SEG technical program expanded abstracts 1998*, 1377–1380, Society of Exploration Geophysicists (doi: 10.1190/1.1820161).

Park CB, Miller RD and Xia J (1999) Multichannel analysis of surface waves. *Geophysics*, **64**(3), 800–808 (doi: 10.1190/1.1444590).

Picotti S, Francese R, Giorgi M, Pettenati F and Carcione JM (2017) Estimation of glacier thicknesses and basal properties using the horizontal-to-vertical component spectral ratio (HVSR) technique from passive seismic data. *Journal of Glaciology*, **63**(238), 229–248 (doi: 10.1017/jog.2016.135).

Podolskiy EA and Walter F (2016) Cryoseismology. *Reviews of Geophysics*, **54**(4), 708–758 (doi: 10.1002/2016RG000526).

Preiswerk LE, Michel C, Walter F and Fäh D (2019) Effects of geometry on the seismic wavefield of alpine glaciers. *Annals of Glaciology*, **60**(79), 112–124 (doi: 10.1017/aog.2018.27).

Redpath BB (1973) Seismic refraction exploration for engineering site investigations. Technical report, Army Engineer Waterways Experiment Station (doi: 10.2172/4409605).

Shragge J, Yang J, Issa N, Roelens M, Dentith M and Schediwy S (2021) Low-frequency ambient distributed acoustic sensing (DAS): Case study from Perth, Australia. *Geophysical Journal International*, **226**(1), 564–581.

Smith AM (1997) Variations in basal conditions on Rutford Ice Stream, West Antarctica. *Journal of Glaciology*, **43**(144), 245–255 (doi: 10.3189/S0022143000003191).

Socco L and Strobbia C (2004) Surface-wave method for near-surface characterization: A tutorial. *Near Surface Geophysics*, **2**(4), 165–185 (doi: 10.3997/1873-0604.2004015).

Stevens NT, Roland CJ, Zoet LK, Alley RB, Hansen DD and Schwans E (2023) Multi-decadal basal slip enhancement at Saskatchewan glacier, Canadian Rocky Mountains. *Journal of Glaciology*, **69**(273), 71–86 (doi: 10.1017/jog.2022.45).

Stevens NT, Zoet LK, Hansen DD, Alley RB, Roland CJ, Schwans E and Shepherd CS (2024) Icequake insights on transient glacier slip mechanics near channelized subglacial drainage. *Earth and Planetary Science Letters*, **627**, 118513 (doi: 10.1016/j.epsl.2023.118513).

Stockwell Jr JW (1999) The CWP/SU: Seismic Unix package. *Computers & Geosciences*, **25**(4), 415–419.

Tsuji T, Johansen TA, Ruud BO, Ikeda T and Matsuoka T (2012) Surface-wave analysis for identifying unfrozen zones in subglacial sediments. *Geophysics*, **77**(3), EN17–EN27 (doi: 10.1190/geo2011-0222.1).

Veitch SA, Karplus M, Kaip G, Gonzalez LF, Amundson JM and Bartholomaus TC (2021) Ice thickness estimates of Lemon Creek Glacier, Alaska, from active-source seismic imaging. *Journal of Glaciology*, **67**(265), 824–832 (doi: 10.1017/jog.2021.32).

Walter F, Roux P, Roeoesli C, Lecointre A, Kilb D and Roux PF (2015) Using glacier seismicity for phase velocity measurements and Green's function retrieval. *Geophysical Journal International*, **201**(3), 1722–1737 (doi: 10.1093/gji/ggv069).

Yang J (2005) Rayleigh surface waves in an idealised partially saturated soil. *Geotechnique*, **55**(5), 409–414 (doi: 10.1680/geot.2005.55.5.409).

Zechmann JM, Booth AD, Truffer M, Gusmeroli A, Amundson JM and Larsen CF (2018) Active seismic studies in valley glacier settings: strategies and limitations. *Journal of Glaciology*, **64**(247), 796–810 (doi: 10.1017/jog.2018.69).

APPENDIX A: ABBREVIATION SUMMARY

Table 3. List of Abbreviations Used Throughout the Manuscript

Initialism	**Full Description**
1-C	Single- or One-Component
3-C	Three-Component
MC	Multi-Component (regarding more than one component)
DC	Dispersion Curve
DP	Dispersion Panel
HVSR	Horizontal-to-Vertical Spectral Ratio
MASW	Multi-Channel Analysis of Surface Waves
P-wave	Compressional Wave
S-wave	Shear Wave
SV-wave	Vertical Shear Wave with particle motion parallel to plane of wave propagation
CC	Complex Conjugate (Component): $Z(d,t) + iR(d,t)$
R	Radial (Component) - along to source-receiver direction
T	Transverse (Component) - counter clockwise from R direction
Z	Vertical (Component)

703 # APPENDIX B: NOTATION SUMMARY

Table 4. List of Notations Used Throughout the Manuscript

Symbol	Description
V_p	Compressional-wave (P-wave) velocity
V_s	Shear-wave (S-wave) velocity
V_r	Rayleigh-wave phase velocity
ρ	Density
U_x	Horizontal particle displacement
U_z	Vertical particle displacement
Φ	Scalar potential associated with P-waves
Ψ	Vector potential associated with SV-waves
A	Amplitude scaling factor
p	Horizontal slowness
$\hat{\eta}_p$	Vertical slowness for P-waves: $\sqrt{1/V_r^2 - 1/V_p^2}$
$\hat{\eta}_s$	Vertical slowness for S-waves: $\sqrt{1/V_r^2 - 1/V_s^2}$
f	Frequency
f_0	Resonant (or fundamental) frequency
ω	Angular frequency: $2\pi f$)
λ	Wavelength: V_r/f
z	Depth
h	Ice thickness
h_r	Depth at which Rayleigh wave particle motion reverses (retrograde to prograde)
L	Array length
Δr_x	Receiver spacing
d	Source-receiver offset
t	Time
$D(d,t)$	Seismic data in shot-gather format
$D(d,\omega)$	Frequency-domain transform of seismic data
$D_N(d,\omega)$	Frequency-domain seismic with normalized trace amplitudes
$D_S(V_r,\omega)$	Dispersion panel format after slant-stack processing

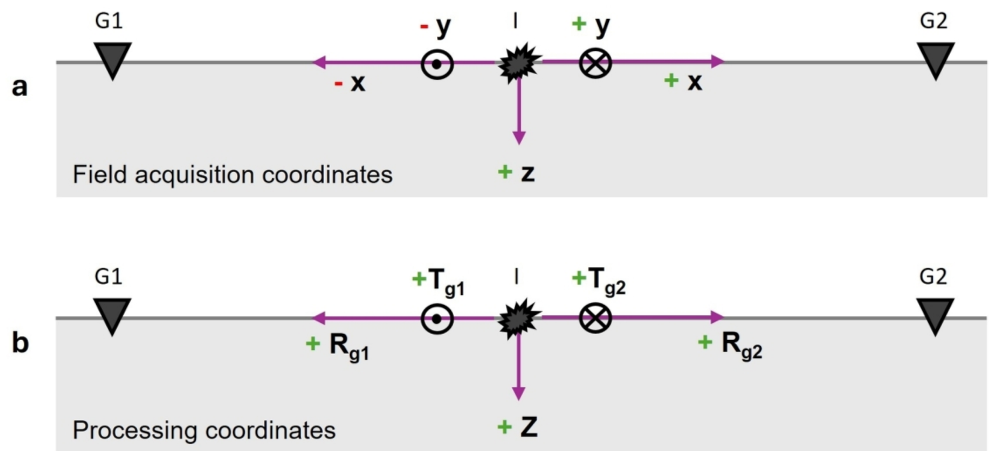

Definition of the (a) acquisition coordinate system in horizontal (x and y) and vertical (z) directions, and (b) the cylindrical processing coordinate system in outward-positive radial R and vertical Z directions. The transverse, T direction is always counter clockwise from R. I and G annotate the locations of the impact source and receivers in each sketch.

152x70mm (300 x 300 DPI)

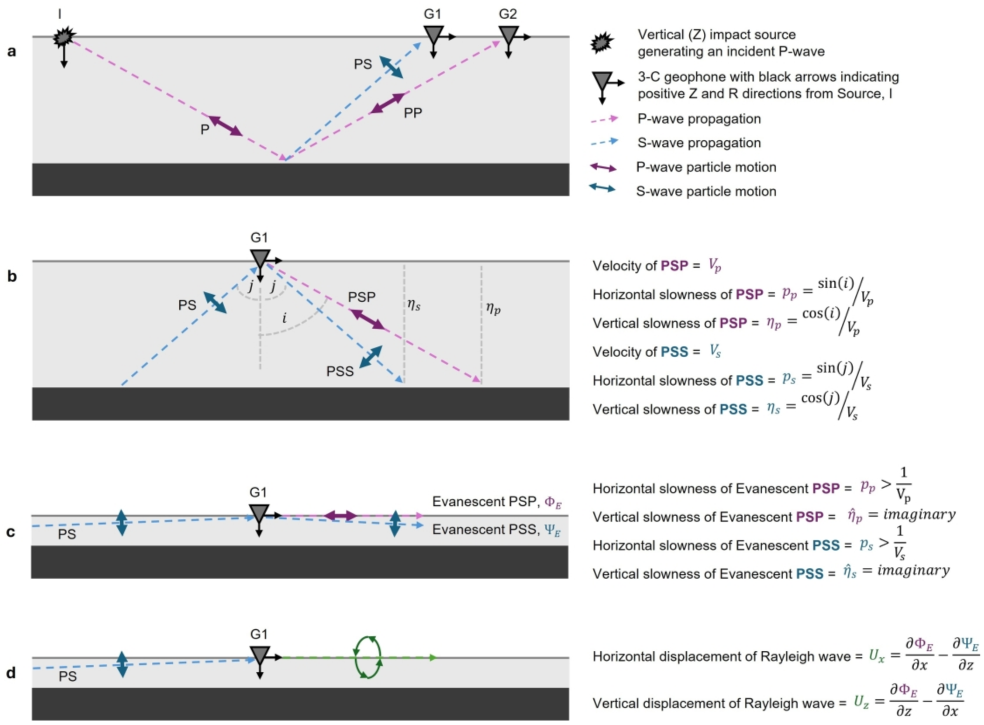

Conceptual representation of Rayleigh-wave generation from a vertical impact source I. (a) An incident P wave reflects off an impedance contrast producing up-going reflected P (PP) and S (PS) waves. (b) The up-going PS wave undergoes total internal reflection at the free surface producing a PSS wave and a mode-converted PSP wave. The velocity and horizontal and vertical slownesses are described relative to the free-surface incidence angle. (c) At large angles of incidence, evanescent PSP and PSS waves propagate along the surface out-of-phase thus producing (d) a Rayleigh wave with retrograde elliptical particle motion along the free surface. U_z and U_x are described in terms of the potentials, Φ and Ψ, of the evanescent wavefields.

278x200mm (300 x 300 DPI)

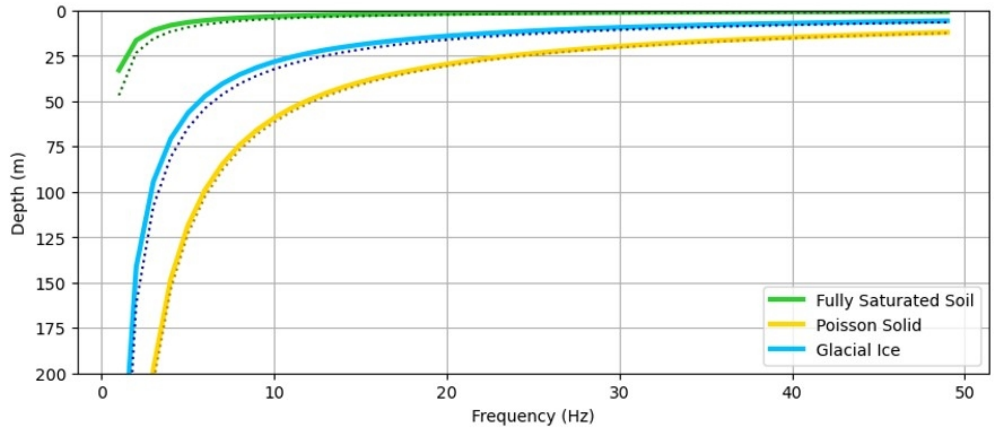

Frequency-dependent depths at which Rayleigh-wave particle motion change from retrograde to prograde for a fully saturated soil profile (green) (Yang, 2005), a Poisson's solid (yellow) (Ammon and others, 2020), and glacial ice (blue) based on parameters estimated for the Saskatchewan Glacier (Stevens and others, 2023). Solid line are analytical solutions (Eqn. (5)), and dotted lines are approximated depths (Eqn. (6)) for all models. Table 1 lists associated material properties.

224x99mm (100 x 100 DPI)

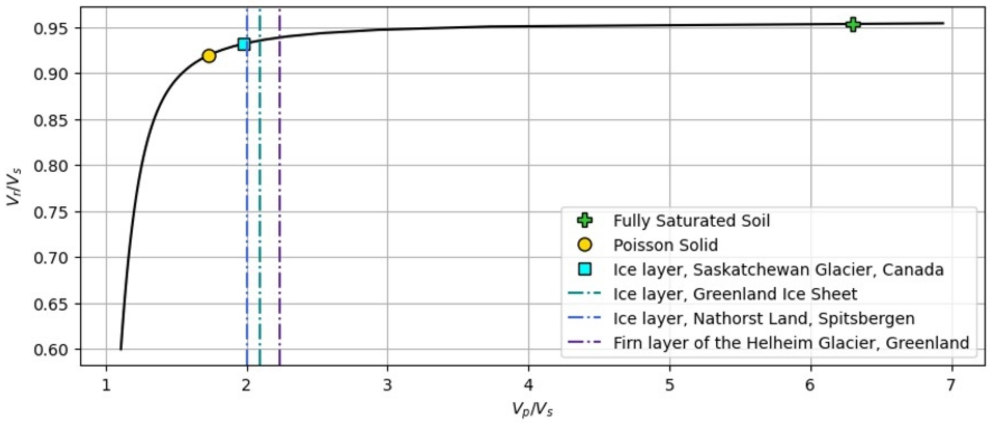

Rayleigh-wave characteristic equation (Eqn. (7)) represented as a relationship between V_p/V_s and V_r/V_s (black curve) with reference values for a saturated soil (green cross), Poisson solid (yellow circle), and glacial ice at the Saskatchewan Glacier (cyan square). V_p/V_s estimates of other glacial examples are plotted as vertical lines since V_r/V_s estimates are not mentioned in reference studies. Table 1 lists associated material properties.

226x99mm (100 x 100 DPI)

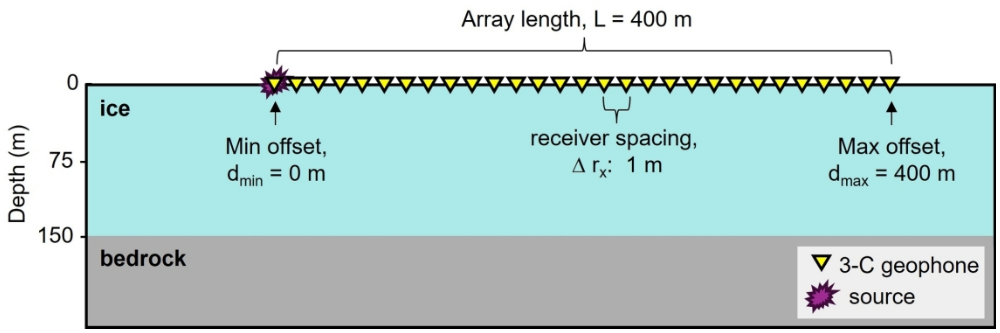

Model describing a homogeneous, isotropic, elastic ice layer of 150 m thickness overlying a bedrock half space. Table 2 presents the elastic model properties. The idealized acquisition has a dense 1 m receiver spacing and 400 m aperture. The sketched geometry is not to scale and approximates receiver placement for visual reference.

189x62mm (300 x 300 DPI)

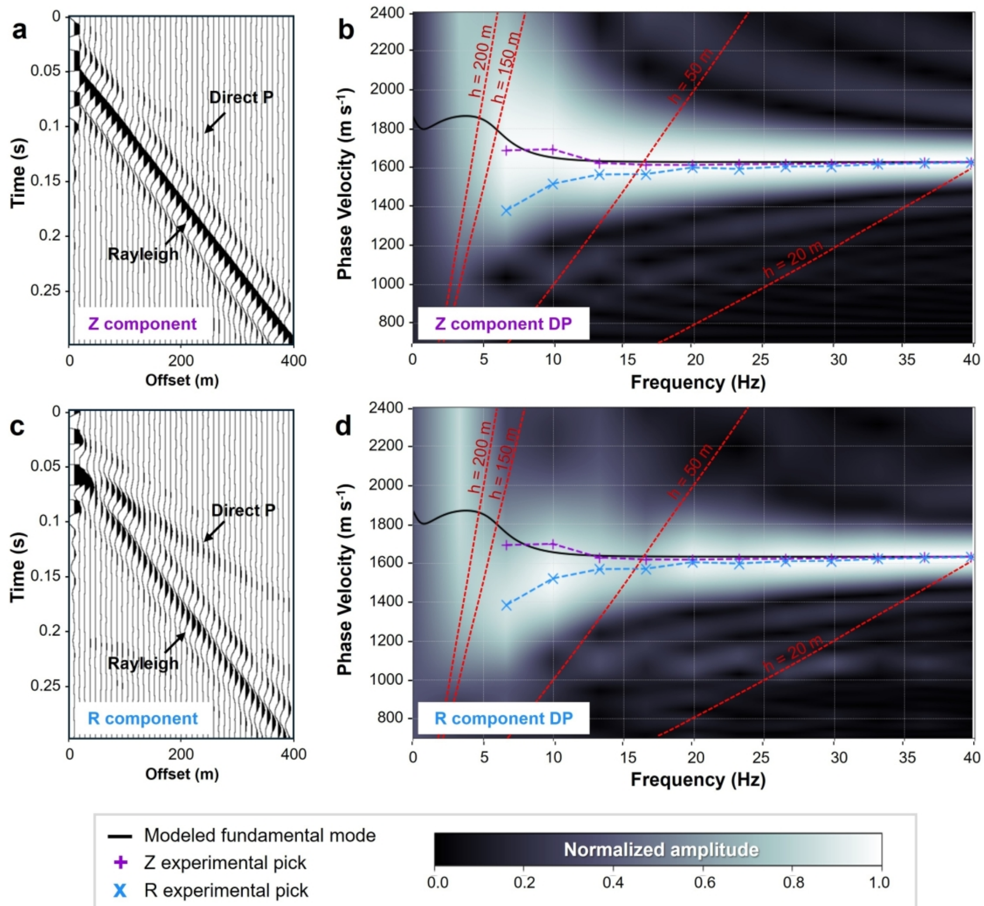

(a) Raw Z-component shot-gather data with corresponding (b) Z-component and (c) raw R-component shot-gather data with corresponding (d) R-component DP for the two-layer ice-bedrock model (Fig. 5), with the numerically calculated DC for the fundamental model (black line). Every 10th trace is shown in the shot gathers for display purposes. Dashed red lines on DPs highlight the maximum wavelengths for resolving depths 20 m, 150 m, and 200 m; valid regions for picking experimental DCs for each depth range fall to the right of these lines. The experimental DCs for the Z- (purple) and R- (blue) components are displayed on both DPs. We note the DC complexity particularly for R and sub-10 Hz Z, which are not consistent with the numerical solution.

225x208mm (300 x 300 DPI)

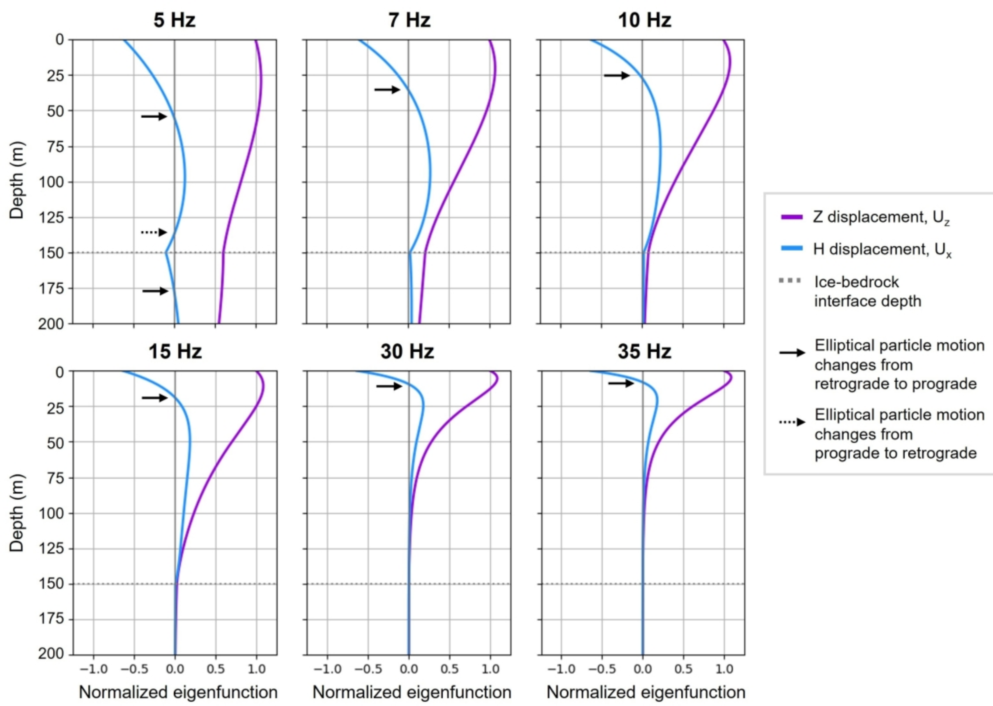

Monochromatic depth-sensitivity kernels for the two-layer homogeneous-ice model (Fig. 5). Curves are the eigenfunctions (the layered-model equivalent of the third terms of equations (1) and (2) normalized to $U_Z(Z=0)=1$) and represent the sensitivity of U_Z (purple) and U_X (blue) components to discrete model depths and wave frequencies. The dotted gray lines show the ice-bedrock interface depth for which only the 5-10 Hz panels show non-zero U_Z sensitivity and only 5-7 Hz show non-zero U_X sensitivity.

238x169mm (300 x 300 DPI)

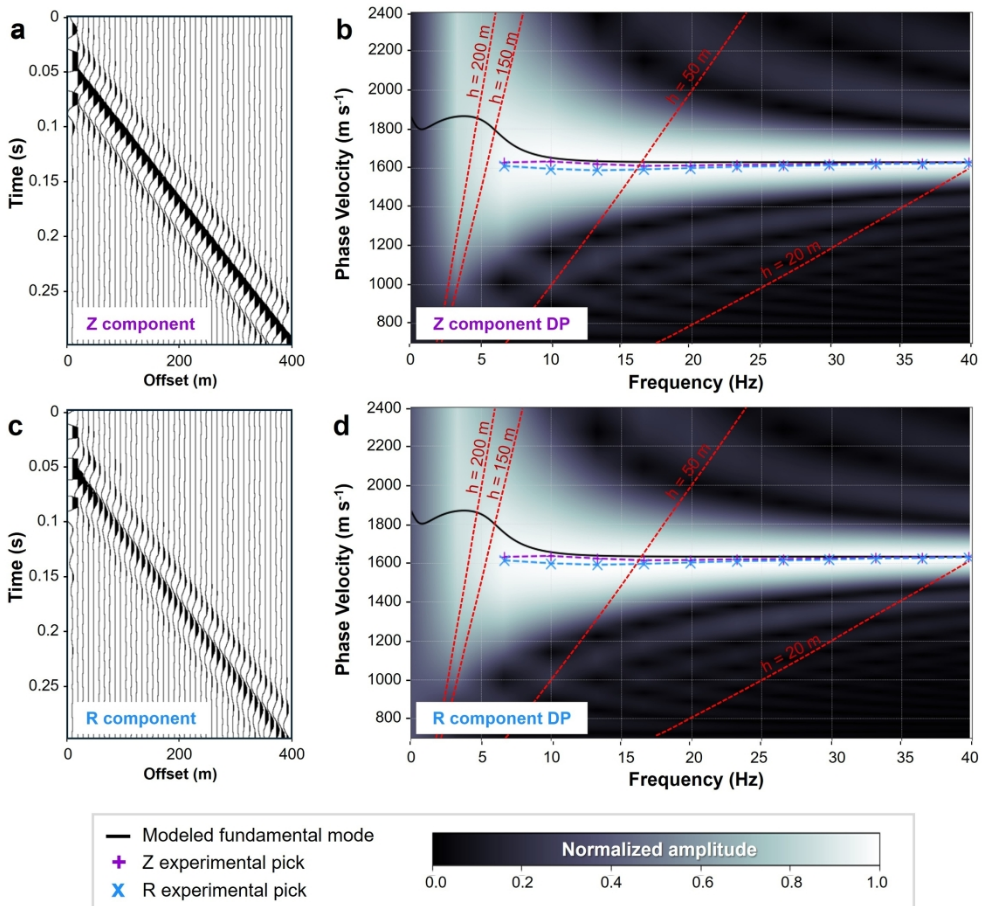

Conditioned shot gathers and DPs after removing the direct P-wave arrivals. See Fig. 6 for descriptions of individual panels. Note the substantial improvement in the continuity of the R-component DPs, with the mean Z- and R-component pick discrepancy reduced from 180 m s^{-1} to 40 m s^{-1}. Additionally, the experimental Z- and R-component picks are more closely aligned to the numerical solution (black line) --- reduced from 130 m s^{-1} to 60 m s^{-1}.

225x208mm (300 x 300 DPI)

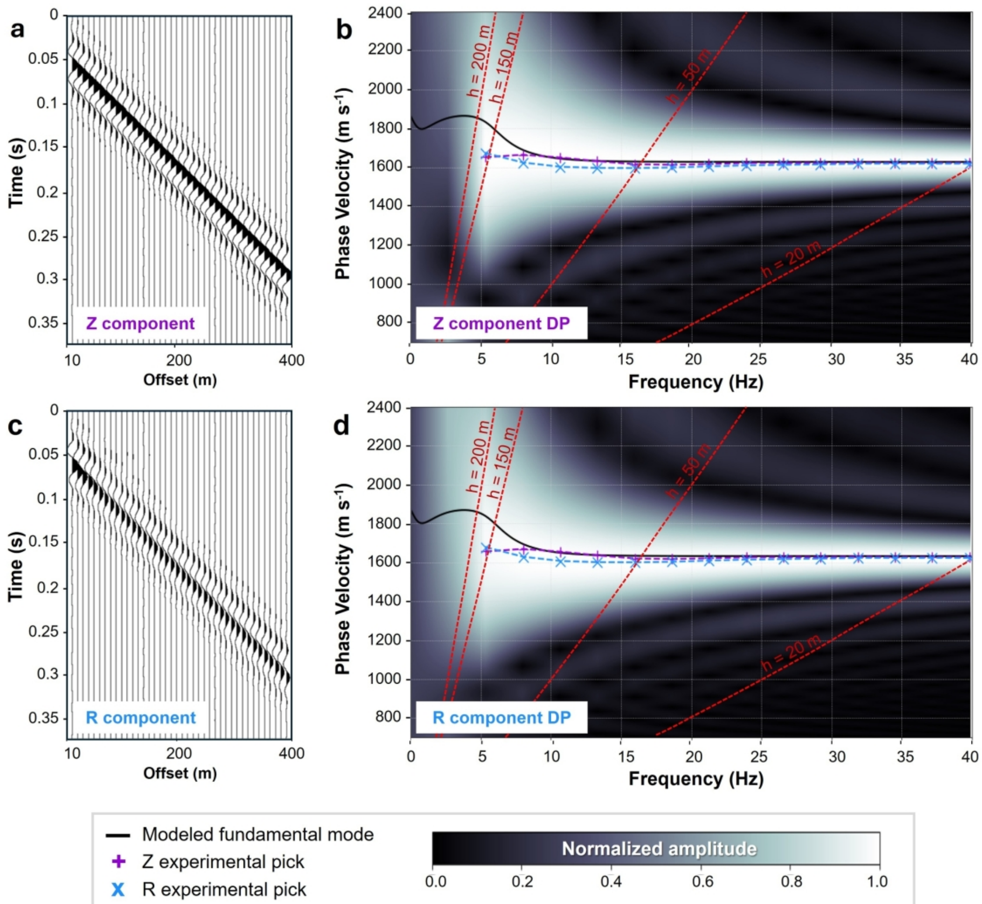

Conditioned shot gather data and DPs after removing the direct P-wave arrival and windowing out noisy near-offset traces to highlight the full Rayleigh-wave character at far offsets. See Fig. 6 for descriptions of individual panels. We improved sub-10 Hz resolution of the DPs with appropriate data conditioning.

225x208mm (300 x 300 DPI)

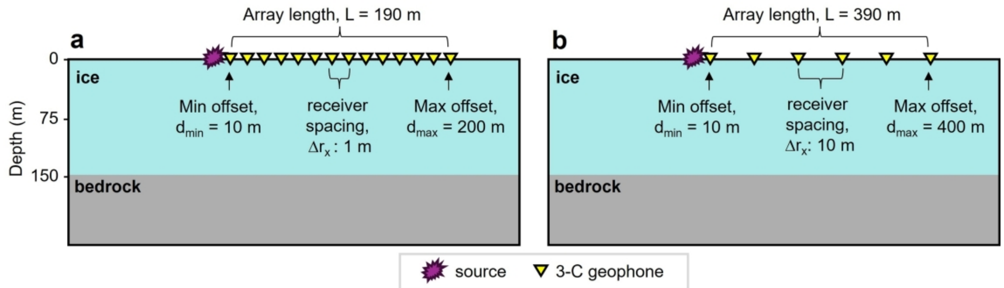

Two-layer ice-bedrock model described in Table 2 with two different acquisition experiments: (a) an aperture of L=190 m (approximately half the length of the example described in Fig. 5) and a receiver spacing of Δr_x=1 m with the zero-offset receiver removed; and (b) an aperture of L=390 m and a receiver spacing of Δr_x=10 m. Not drawn to scale with the receiver placement only approximate for visual reference.

246x72mm (300 x 300 DPI)

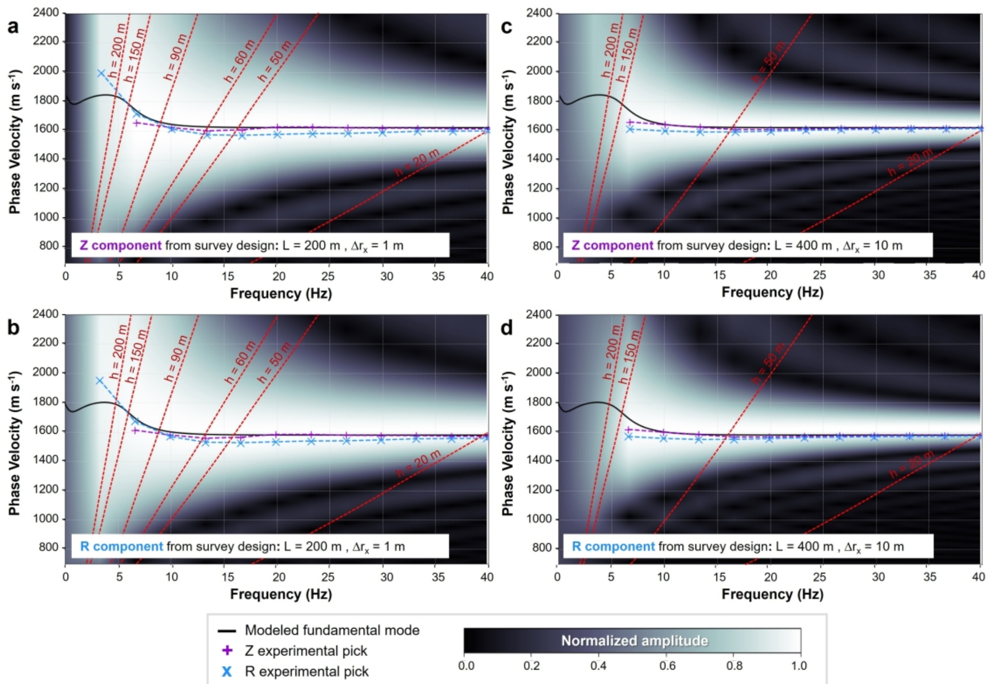

Dispersion panels for Z- and R-component data from the two experiments described in Fig. 10. We conditioned data by removing the direct P-wave arrival and windowing to capture the full Rayleigh-wave signal at all offsets. (a) Z- and (b) R-component dispersion panels for shorter aperture (L=190 m) experiment with dense (Δr_x=1 m) receiver sampling; The resulting dispersion panels are lower resolution compared to the those generated from the ideal acquisition (Fig. 9). (c) Z- and (d) R-component dispersion panels for longer aperture experiment (L=390 m) with sparse (Δr_x=10 m) receiver sampling showing comparably lower data distortion than for the limited aperture case.

298x206mm (300 x 300 DPI)

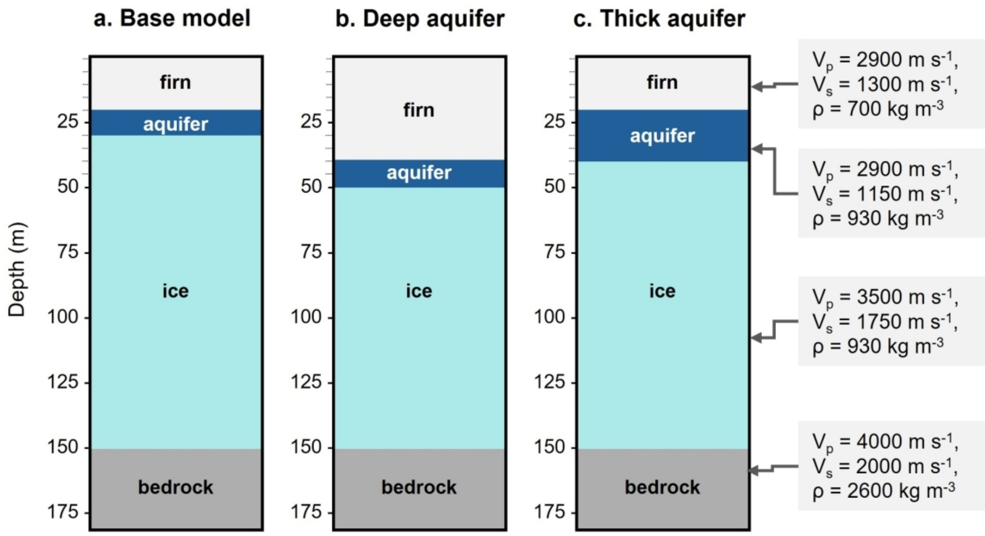

Firn-aquifer model variations for synthetic data generation. (a) ``Base'' model derived from Helheim Glacier seismic inversion results (Killingbeck and others, 2018) with a 10 m thick aquifer overlain by 20 m of firn and a bedrock half-space imposed at 150 m depth. (b) ``Deep Aquifer" model similar to (a) but with the firn layer extended to a depth of 40 m. (c)``Thick Aquifer" model similar to (a) but with the aquifer thickened to 20 m.

180x96mm (300 x 300 DPI)

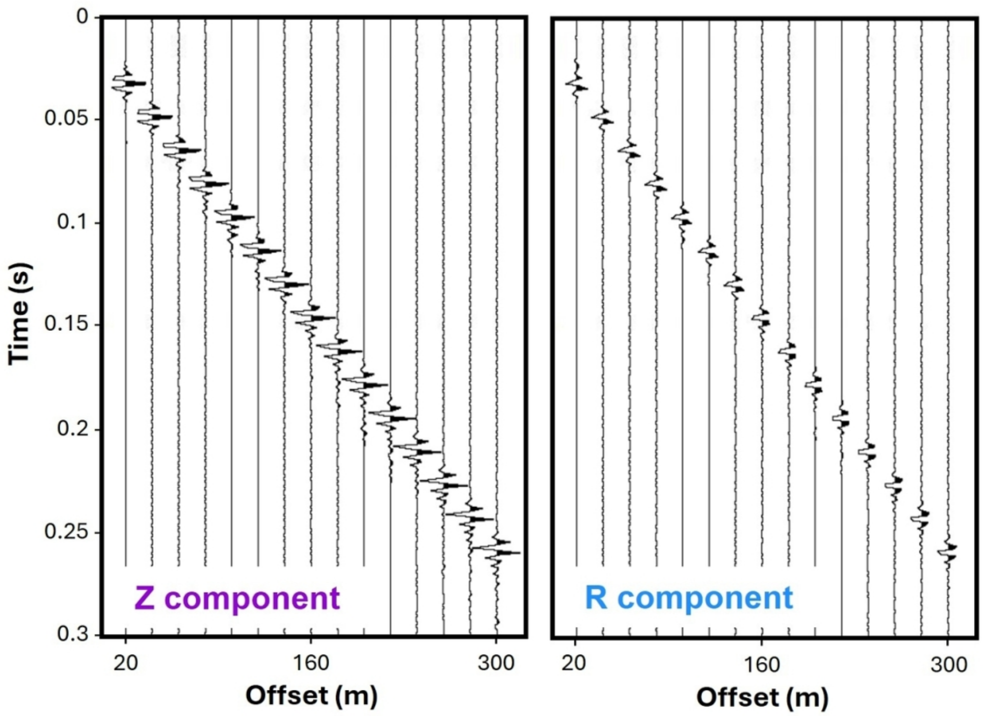

Conditioned Z- and R-component shot gathers for the ``base'' firn-aquifer model described in Fig. 12. Every 20th trace is plotted for offsets ranging from 20 m to 300 m.

118x88mm (300 x 300 DPI)

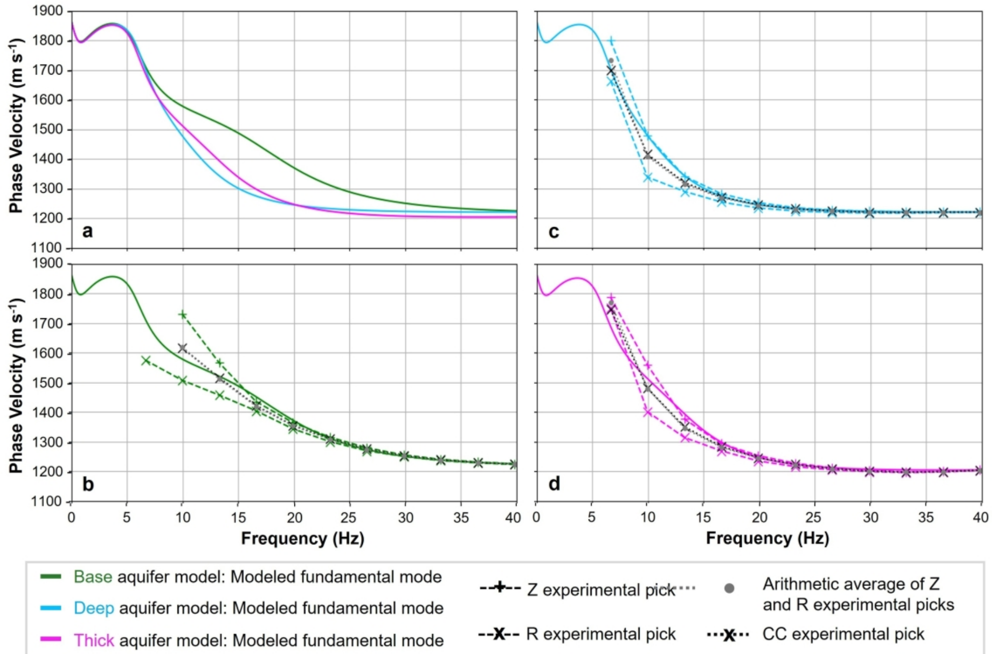

Numerical solutions and experimental DCs of the fundamental mode associated with the three models described in Fig. 12. (a) Numerical solution of the fundamental DC for base (green), deep aquifer (cyan), and thick aquifer (magenta) models. Z- and R-component DCs for the (b) base, (c) deep aquifer, and (d) thick aquifer models, with experimental picks for Z- (plus symbols) and R-component (cross symbols), the arithmetic average of Z- and R-component phase velocity (grey circles), and the complex conjugate (CC) of Z- and R- components (black cross symbols). Between 8 and 20 Hz, the variability of DCs for the three models suggests that accurate picks in this frequency band are important for mitigating the non-uniqueness of dispersion analysis and inversion.

246x163mm (300 x 300 DPI)

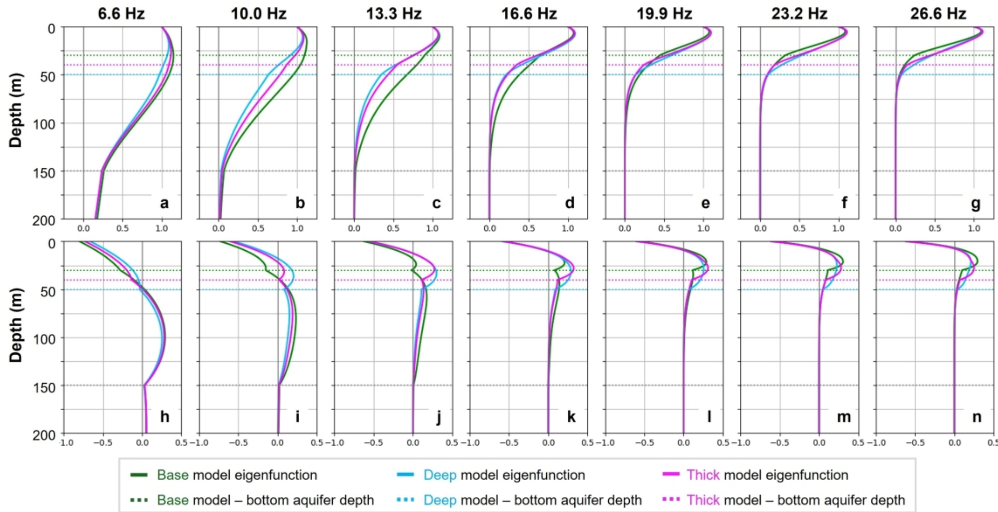

Depth sensitivity kernels for discrete frequencies of the three aquifer-firn experiments described in Fig. 12. (a--g) U_z components. (h--n) U_x components. Depths of the bottom of aquifer are color coded for each model, and the depth of the ice-bedrock interface is shown with a dotted gray line at 150 m. The unique sensitivities of the U_x curves for each model motivate an opportunity for improving MASW inversion accuracy through use of MC data.

302x157mm (300 x 300 DPI)

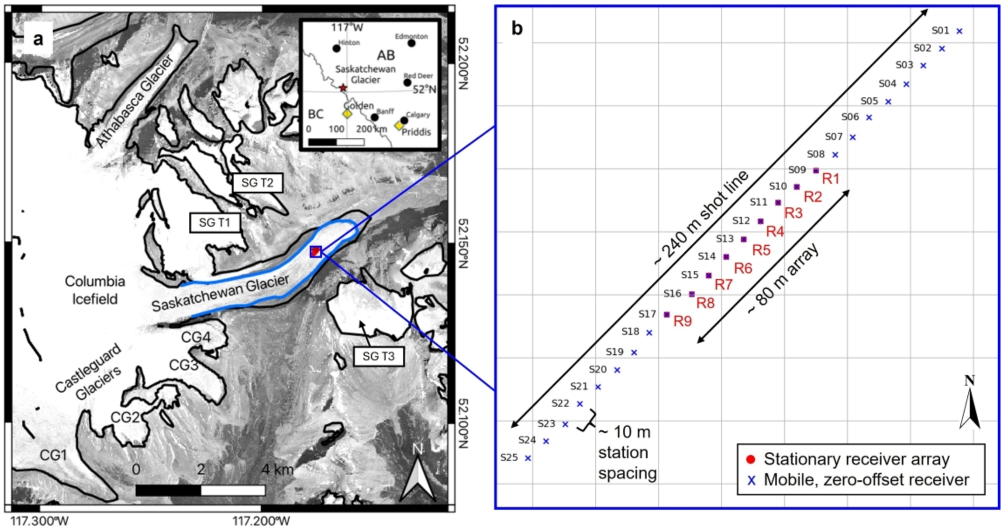

(a) Saskatchewan Glacier location in the Canadian Rocky Mountains, Canada (see inset map). Basemap imagery: Orthorectified 4-band PlanetScope scene accessed via Planet.com (b) Geometry of the active-source seismic experiment conducted in the ablation zone involving a stationary array of nine 3-C geophones (R1-R9) linearly spaced at 10 m to form an array of aperture L=80 m. Source station locations S01-S25, also spaced 10 m apart, are shown as blue Xs.

288x153mm (300 x 300 DPI)

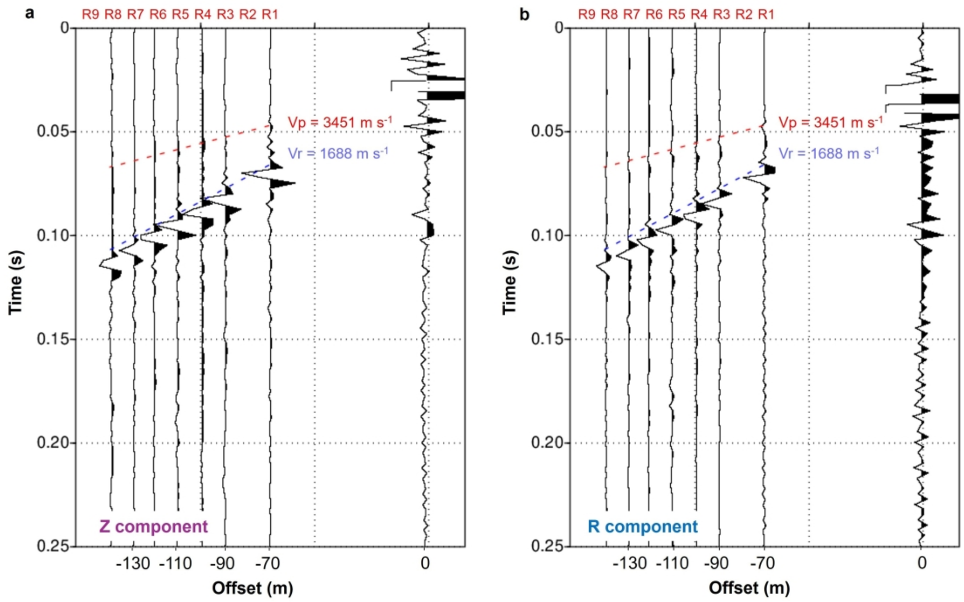

(a) Raw Z- and (b) R-component shot-gather data for station S02. The zero-offset trace recorded by the mobile geophone is used to window the continuously recorded data on geophones R1-R9 into shot gathers. V_p and V_r moveout velocities calculated by Stevens and others, 2023 are plotted. Note the missing traces at R2 and R9. Additionally, direct P-wave arrival is weaker on the Z- versus the R-component because of the predominantly horizontal particle motion. Strong Rayleigh wave energy is recorded on both components.

284x174mm (300 x 300 DPI)

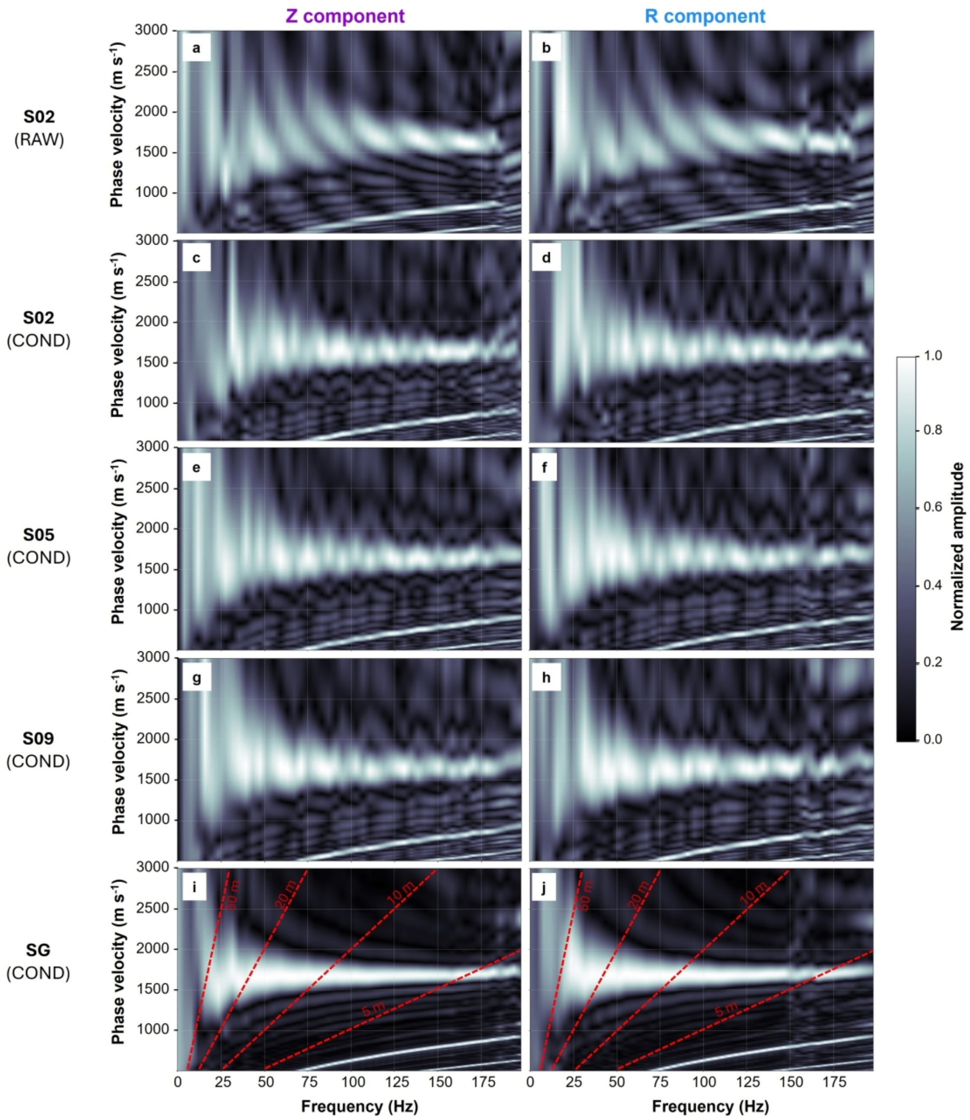

Raw (a) Z- and (b) R-component DPs for the S02 shot gathers shown in Fig. 17. Conditioned (c) Z- and (d) R-component DPs corresponding to (a) and (b) after removing the zero-offset traces, muting the direct wave, and infilling missing traces with a zeroed trace. Conditioned (e) Z- and (f) R-component DPs at station S05 and (g) Z- and (h) R-component for station S09. Conditioned (i) Z- and (j) R-component supergather DPs combining S02, S05, and S09 shot-gather data. The conditioned individual shots produce consistent DCs although a beat-like signature is imposed as a result of the zeroed infill trace and no interpolation. The supergather DC infills missing offsets and extends the effective array aperture producing higher-resolution DPs.

260x292mm (300 x 300 DPI)

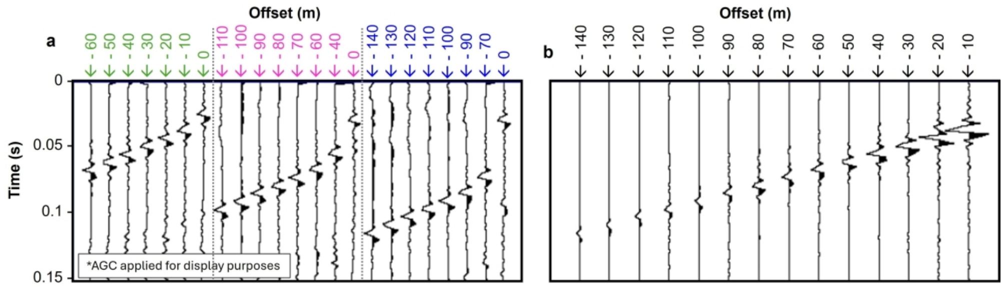

(a) Time-aligned Z-component shot gathers for stations S02 (blue), S05 (pink), and S09 (green) with differing offset ranges (x-axis labels). (b) Supergather produced from stacking the three shots in (a) based on similar offsets thus increasing the effective array aperture to L=130 m and infilling missing offset traces without interpolation.

323x95mm (300 x 300 DPI)

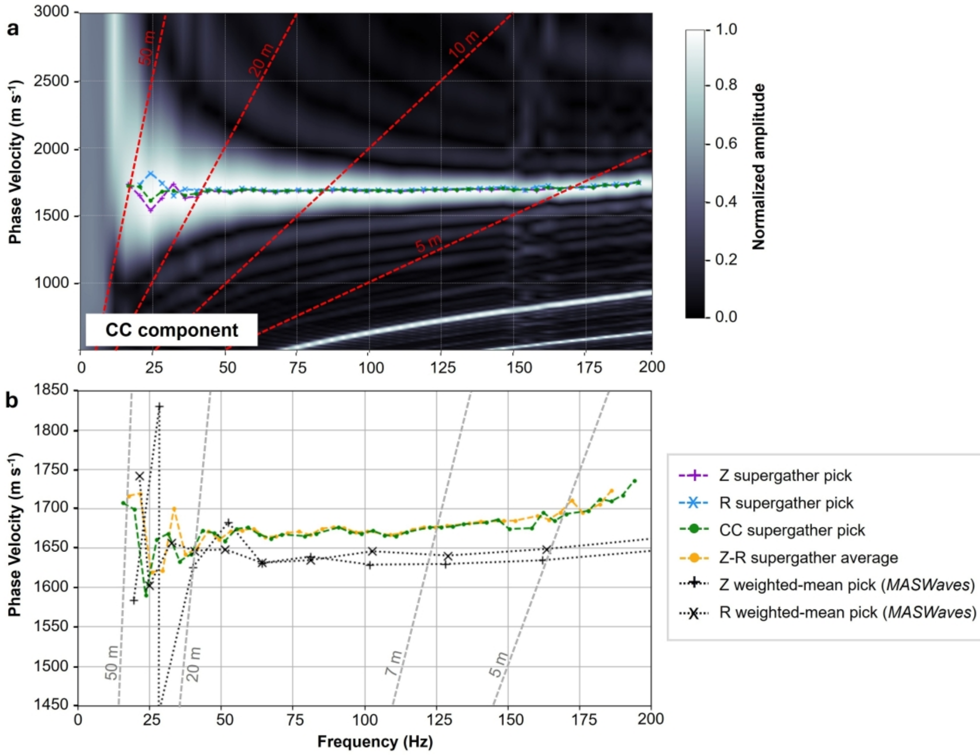

(a) Dispersion panel derived from CC supergather from shots 02, 05 and 09. (b) Comparison of experimental dispersion curve picks from CC supergather (dashed black line) and individual Z- and R-components (+ and x symbols, respectively), the arithmetic mean (black dots), and the weighted-mean picks calculated from the internal *MASWaves* algorithm (dark and light purple for Z and R components, respectively). All picks were made on the respective DC panels (Fig. 18) using the standard picking algorithm in the *MASWaves* software. There is little evidence of dispersion and the experimental picks suggest an average V_r=1670 m s^{-1} between 40 and 165 Hz.

263x201mm (300 x 300 DPI)